

AN INSTRUMENT TO MEASURE THE TWO-DIMENSIONAL
WAVE SLOPE SPECTRUM OF OCEAN CAPILLARY WAVES

By

CHARLES SHELBY PALM

A DISSERTATION PRESENTED TO THE GRADUATE COUNCIL OF
THE UNIVERSITY OF FLORIDA
IN PARTIAL FULFILLMENT OF THE REQUIREMENTS FOR THE
DEGREE OF DOCTOR OF PHILOSOPHY

UNIVERSITY OF FLORIDA

1975

Dedicated to
JESSE ALBERT GOODE, M.D.

ACKNOWLEDGEMENTS

I am thankful for the support provided by the members of my Supervisory Committee. Special thanks are due to Dr. R. C. Anderson for suggesting the project, Dr. O. H. Shemdin for providing the funding, and Dr. D. T. Williams for providing encouragement and guidance throughout my stay at the University. Mr. Harry Stroud was instrumental in material acquisition and was generally invaluable in seeing the project to a successful completion. Mr. Allan Reece generously applied many hours of his own time to this project. His suggestions were helpful and his expertise with the wave tank facility controls and the IBM 370 computer helped to reduce the total project time considerably. I am also grateful to my wife, Emelyn, for the many hours she spent typing this paper.

TABLE OF CONTENTS

ACKNOWLEDGEMENTS	iii
LIST OF FIGURES	v
ABSTRACT	viii
CHAPTER I, INTRODUCTION	1
CHAPTER II, DESCRIPTION OF THE INSTRUMENT	3
Theory of Operation	3
Optical Design	6
Description of Instrument Components	9
CHAPTER III, THEORETICAL PERFORMANCE AND OPERATING CHARACTERISTICS OF THE INSTRUMENT	27
Introductory Remarks	27
Wavelength Response Characteristics	35
CHAPTER IV, WAVE TANK TEST	56
CHAPTER V, OCEAN TEST	61
CHAPTER VI, SUMMARY	66
CHAPTER VII, CONCLUDING REMARKS	67
REFERENCES	68
BIOGRAPHICAL SKETCH	70

LIST OF FIGURES

Figure 1:	Geometry associated with the refraction of a ray of light at a water-air interface.	5
Figure 2:	Paraxial design of the optical system.	7
Figure 3:	The optical receiver portion of the waveslope instrument.	10
Figure 4:	Performance curve for the objective lens.	12
Figure 5:	The imaging lens module.	14
Figure 6:	Two-dimensional Schottky Barrier Photodiode.	16
Figure 7:	Electronic amplifiers.	18
Figure 8:	Block diagram of the electronic amplifier.	19
Figure 9:	Schematic diagram of one amplifier channel.	20
Figure 10:	Illustration of the effectiveness of the analog dividers to produce a normalized signal voltage.	22
Figure 11:	The oceangoing support structure.	25
Figure 12:	Sketch of the wave slope instrument during ocean operation.	26
Figure 13:	The calibration set up in the optical laboratory.	29
Figure 14:	A typical plot of calibration data obtained using the analog divider.	30

LIST OF FIGURES (continued)

Figure 15: Offset voltages measured with respect
to the amplifier outputs. 32

Figure 16: Photographs showing the location of
the optical-tube thermometer relative
to the amplifiers in the imaging lens
module. 33

Figure 17: Configuration for the i^{th} -wave
component and the Gaussian
laser beam. 40

Figure 18: Approximation to the Gaussian
intensity distribution used
in the computer error analysis. 44

Figure 19: λ/r_0 as a function of the parameter k/σ 47

Figure 20: Error in the waveslope measurement,
 ϵ , as a function of parameter k/σ at $wt = 0$
for various values of parameter ak 48

Figure 21: Percent error in wave slope
measurement as a function of
parameter k/σ , for $wt = 0$ and $ak = 5^\circ, 45^\circ$ 49

Figure 22: Error in wave slope measurement, ϵ , as
a function of wave phase, for
various values of maximum wave slope
and for $k/\sigma = 0.7$ ($\lambda/r_0 = 6.34$). 51

Figure 23: Sample records from the wave tank tests. 57

Figure 24: Frequency spectra of the mean square slope. 59

LIST OF FIGURES (continued)

Figure 25: Photograph of shrimp boat's position relative to the ocean test site.	62
Figure 26: The instrument in operation during the ocean test.	63
Figure 27: Sample records of ocean test data.	64

Abstract of Dissertation Presented to the Graduate Council
of the University of Florida in Partial Fulfillment of the Requirements
for the Degree of Doctor of Philosophy

AN INSTRUMENT TO MEASURE THE TWO-DIMENSIONAL
WAVE SLOPE SPECTRUM OF OCEAN CAPILLARY WAVES

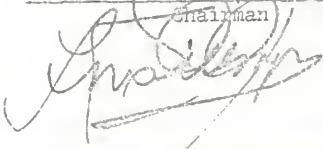
By

Charles Shelby Palm

August, 1975

Supervisory Chairman: Roland C. Anderson
Major Department: Engineering Sciences

An optical instrument for use in determining the two-dimensional wave slope spectrum of ocean capillary waves is described. The instrument measures up to a 35° tip angle of the surface normal by measuring the position of a refracted laser beam directed vertically upward through the water surface. High quality optical lenses, a continuous two-dimensional Schottky barrier photodiode, and a pair of analog dividers render the signals independent of water height and insensitive to laser beam intensity fluctuations. Calibration is performed entirely in the laboratory. Sample records and wave slope spectra are shown for one-dimensional wave tank tests. Sample records of two-dimensional ocean tests are presented. A mechanical wave follower mechanism was used to adjust the instrument's position in the presence of large ocean swell and tides. Errors due to use of a finite-sized laser beam are discussed.


Chairman


CHAPTER I INTRODUCTION

Statistical descriptions of typical shapes of the sea surface and its changes with time are useful in many studies. The study of the effective forces governing the interactions between wind and water led Cox to examine the statistics of small capillary waves.¹ As Cox points out, the shape parameter used in the study of small, high frequency waves is the wave slope. This is so because small wavelength waves have small amplitudes which become difficult to measure accurately as the wavelength decreases. However, these same waves may have wave slopes of considerable magnitude.

The surface slope statistics have been useful in studies relating to the behavior of surface waves in the presence of internal waves, the resonant interaction among capillary waves, backscattering and radiative transfer of electromagnetic radiation in connection with remote sensing of the state of the sea, and relations between a roughened sea surface and multipath effects in communications between satellites and aircraft flying over the ocean.²⁻⁸

Optical methods of measuring waveslopes seem to be popular because the water surface is left undisturbed by the measurement, and the instrumentation required to make the measurement is basically simple, at least in concept. Some of the optical methods used in waveslope studies are based on the principle of measuring reflected light. These schemes include the measurement of light reflected from an artificial source

and light reflected from the sky, and the observation of sun-glitter patterns on the open sea surface.^{9,2,10,11} Other optical methods of wave slope measurement are based on the principle of refraction of light at a surface of the water where a discontinuity in the index of refraction exists. Measurements based on the refraction of light have used both continuous, extended light sources and highly localized light sources in the form of a laser beam.^{1,12,13}

The instrument described in this paper is a second generation development of the one described by Tober et al.¹² The new instrument was designed for and used in both laboratory and oceangoing field tests to measure the two-dimensional wave slope at a point as a function of time.

CHAPTER II
DESCRIPTION OF THE INSTRUMENT

Theory of Operation

The orientation of the surface normal of an elemental area on the surface of a water-air interface may be established by measuring the angle of refraction of a light ray passing through the interface. The relationship between the incident ray and the refracted ray is given by Snell's Law:

$$(1) \quad n_i \sin \theta_i = n_r \sin \theta_r$$

where n_i is the index of refraction for the medium containing the incident ray, n_r is the index of refraction for the medium containing the refracted ray, and θ_i and θ_r are the angles of incidence and refraction, respectively. By defining a deflection angle, ϕ as

$$(2) \quad \phi = \theta_r - \theta_i$$

and using Snell's Law as expressed in equation (1), the deflection angle, ϕ , may be expressed in terms of n and θ_i as

$$(3) \quad \phi = \arcsin (n \sin \theta_i) - \theta_i$$

where n is the relative index of refraction, defined as $n = n_i/n_r$.

Using the direction of the incident ray as a reference direction, the deflection angle, ϕ , may be used to measure the refraction of the incident ray. By aligning the incident ray with the surface normal under calm-water conditions, the angle of incidence, θ_1 , may be related to the angular displacement of the surface normal from the calm-water surface normal orientation, θ , by

$$(4) \quad \theta_1 = \theta .$$

Figure 1 shows the geometry corresponding to the situation described above. Thus, substituting equation (4) into equation (3), the expression for ϕ becomes¹²

$$(5) \quad \phi = \arcsin (n \sin \theta) - \theta .$$

The inverse relation which expresses θ as a function of ϕ is readily found to be

$$(6) \quad \theta = \arctan \left[\frac{\sin \phi}{n - \cos \phi} \right] .$$

Thus it is seen that the measurement of the wave slope, θ , results from a measurement of the deflection angle, ϕ , provided the relative index of refraction, n , is known. Throughout this paper the value for n is taken as $n = 1.333$.

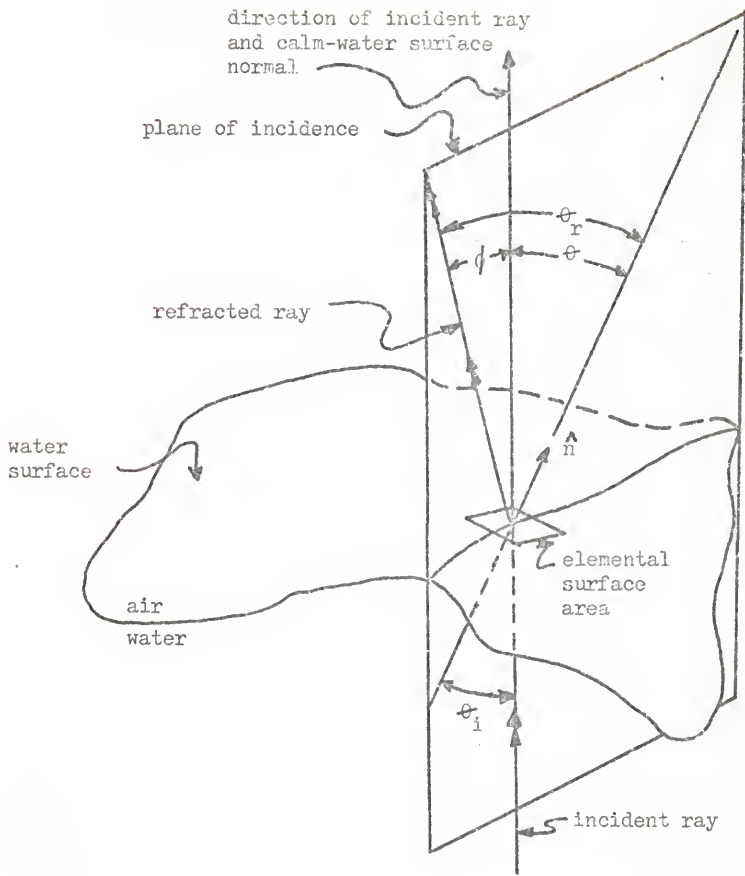


Figure 1: Geometry associated with the refraction of a ray of light at a water-air interface. The wave slope is defined as the angle θ .

Optical Design

The initial Gaussian or paraxial design of the optical components for the wave slope instrument was completed in late May, 1974. The system was designed to measure wave slopes of magnitude up to 45° using a United Detector Technology SC/50 Photodiode as a two-dimensional light-to-electrical signal transducer. Matrix methods of ray-tracing were employed to give the first-order system design shown in Figure 2.¹⁴ The optical receiver portion of the instrument consisted of three lenses and the photodiode transducer.

In the ideal case, the laser beam was assumed to be collimated perfectly and focused to a point at the focal plane by the objective lens. The position of each ray in the back focal plane of the objective lens is determined using a linear transformation

$$(7) \quad \rho = a \phi$$

where ρ is the radial displacement of the focused laser beam from the optical axis, a is a constant which is determined from the lens parameters such as surface curvatures, index of refraction of the lens material, and the thickness of the lens, and ϕ is the angle of deflection of the laser beam from the optical axis. An expression for ϕ in terms of the wave slope, θ , was given earlier in equation (5). The azimuthal angle, ψ , is unaltered in the transformation. Thus it is seen that any light ray entering the objective lens having a deflection angle ϕ and azimuthal direction ψ is directed to a point (ρ, ψ) in the back focal plane of the objective lens. This occurs for every ray entering the

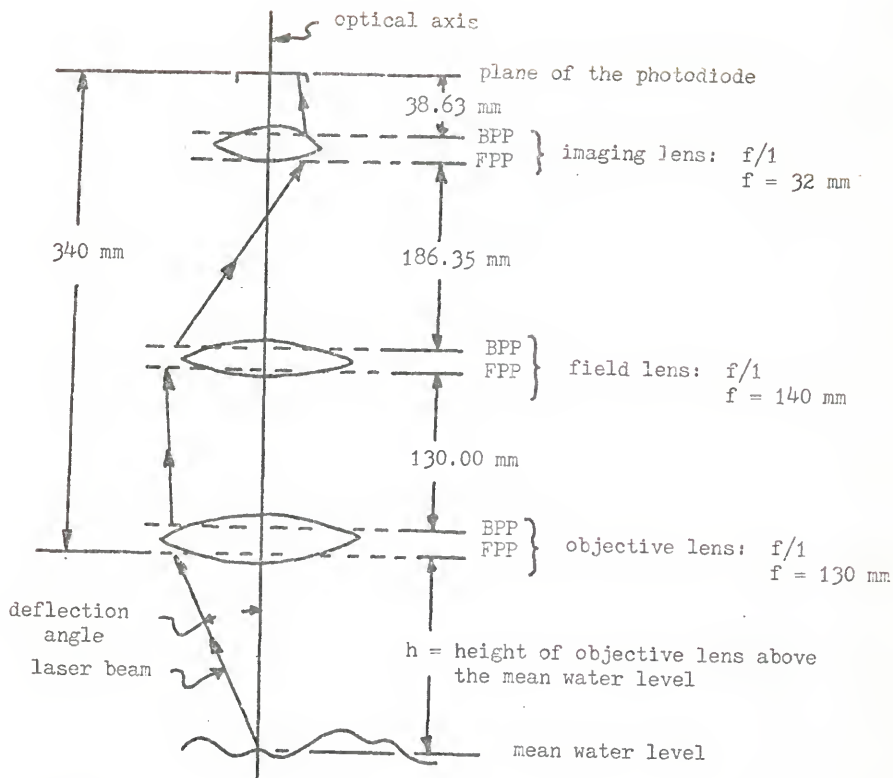


Figure 2: Paraxial design of the optical system.
 The laser beam enters the objective lens and is focused 130 mm from the back principal plane (BBP). The front principal plane (FPP) of the field lens is located at the back focal plane of the objective lens. The field lens confines the laser beam to the optical tube dimensions. The imaging lens images the field lens FPP onto the photodiode surface.

objective lens, regardless of the point of incidence on the first surface of the objective lens. Since a unique point in the focal plane (ρ, ψ) corresponds to a unique ray orientation (ϕ, ψ) , and since ϕ is uniquely related to the wave slope, θ , via equation (5), it is clear that measurement of the position the laser beam in the focal plane (ρ, ψ) gives unambiguous information about the orientation of the water surface normal. Thus the problem of wave slope measurement is essentially solved in the back focal plane of the objective lens.

Although the necessary wave slope information was displayed in the back focal plane of the objective lens, it was necessary to reduce the size of the information-laden portion of the focal plane to match the dimensions of available photodiode transducers. This was accomplished by using a field lens to confine the laser beam within the dimensions of the optical tube and an imaging lens which formed an image of the back focal plane of the objective lens on the active surface of the photodiode. Each of the lenses shown in Figure 2 was to consist of one or more lens elements to correct for optical aberrations.

The system described above was never fabricated because a test-schedule time constraint did not allow enough time to have the elements ground, tested, and assembled. Therefore, the design was modified so that off-the-shelf optical components could be used. The imaging-lens requirement was filled by selecting a high quality 35mm camera lens. An objective lens was selected after six weeks of testing a variety of different commercially available lenses. The one selected was a military surplus aerial camera lens, a 12", f/2.5 Aero-Ektar. It was found to be capable of measuring 35° wave slopes, displayed negligible aberration errors, and had a large enough clear aperture to allow measurements

to be made with the objective lens at a reasonable height above the water surface. A suitable field lens was located, but an excessively long lead time for delivery led to the use of a diffusion screen in place of a field lens. The diffusion screen had the advantages of being lighter in weight and easier to mount in the optical tube, but had the disadvantage of scattering most of the light outside of the imaging lens. The light flux onto the photodiode was thus lowered by approximately two orders of magnitude, and additional electronic amplifier stages were necessary to produce a satisfactory signal. The following section describes the components used to construct the instrument.

Description of Instrument Components

Figure 3a shows a phantom view of the optical receiver portion of the wave slope instrument corresponding to the original design concept. Figure 3b shows a view of the final configuration, and Figure 3c is a photograph of the assembled unit. Brief descriptions of each of the major components and comments on their operating characteristics are given in the following paragraphs. Unless otherwise stated, the physical location of the individual components is indicated in Figure 3.

Objective Lens

For a given height, h , above the water surface, the maximum measurable deflection angle of the laser beam, ϕ_{\max} is dictated by the clear aperture of the objective lens, d , according to the relation

$$(8) \quad \phi_{\max} = \arctan(1/2(h/d)) \quad .$$

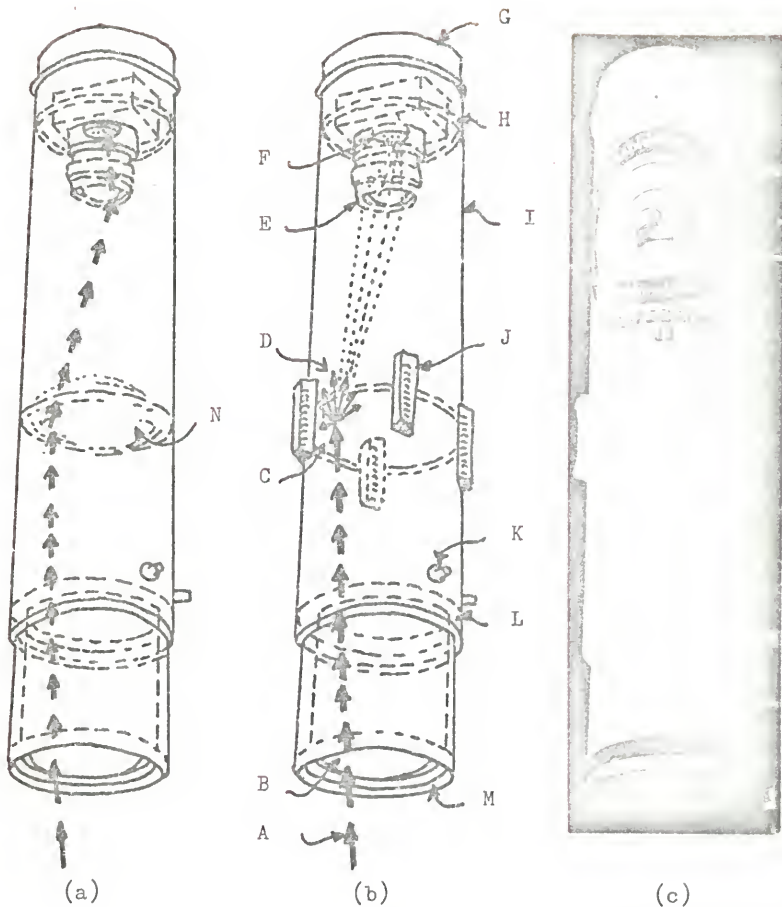


Figure 3: The optical receiver portion of the waveslope instrument. (a) original concept, (b) final configuration, (c) assembled unit. Components: laser beam, A; objective lens, B; diffusion screen, C; scattered laser light, D; imaging lens, E; two-dimensional photodiode, F; tube end cap, G; imaging module mount, H; optical tube, I; diffusion screen adjustment screws, J; N₂ purge lines, K; main support collar, L; plate glass window, M; field lens, N.

A number of commercially available lenses were tested on an optical bench to determine ϕ as a function of the ratio (h/d) . A military surplus aerial camera lens, an Aero-Ektar, $f/2.5$, 12" focal length lens, was selected as being the most suited to the intended purpose of the wave slope instrument. A special lens element support was fabricated for the lens to reduce the total weight from 18.75 lbs to 11 lbs. Figure 4 shows the maximum measurable deflection angle, ϕ_{\max} , as a function of the objective lens height above the water surface, h . Scales indicating the maximum measurable wave slope, θ_{\max} , and the ratio (h/D) , where D is the maximum diameter of the lens barrel at the plane of the first element of the objective lens, are also shown in Figure 4.

The shape of the back focal surface of the objective lens was determined by a series of Foucault knife-edge tests. The surface showed considerable curvature at large displacements from the optical axis, but a plot of the radial displacement of the focal point of the laser beam as a function of the deflection angle, ϕ , was linear to a good approximation. The results indicated that the linear transformation expressed in equation (7) was accurate to within 0.5% or less and a Gaussian or paraxial model of the objective lens was indeed a good approximation. This notion was reinforced later by the results of the calibration tests and the measurement of errors due to optical aberrations.

Diffusion Screen

The diffusion screen was used in place of a field lens because a satisfactory lens could not be procured at the time of instrument fabrication. The diffusion screen served to scatter light from the focused laser beam, thus allowing a sufficient quantity of light to

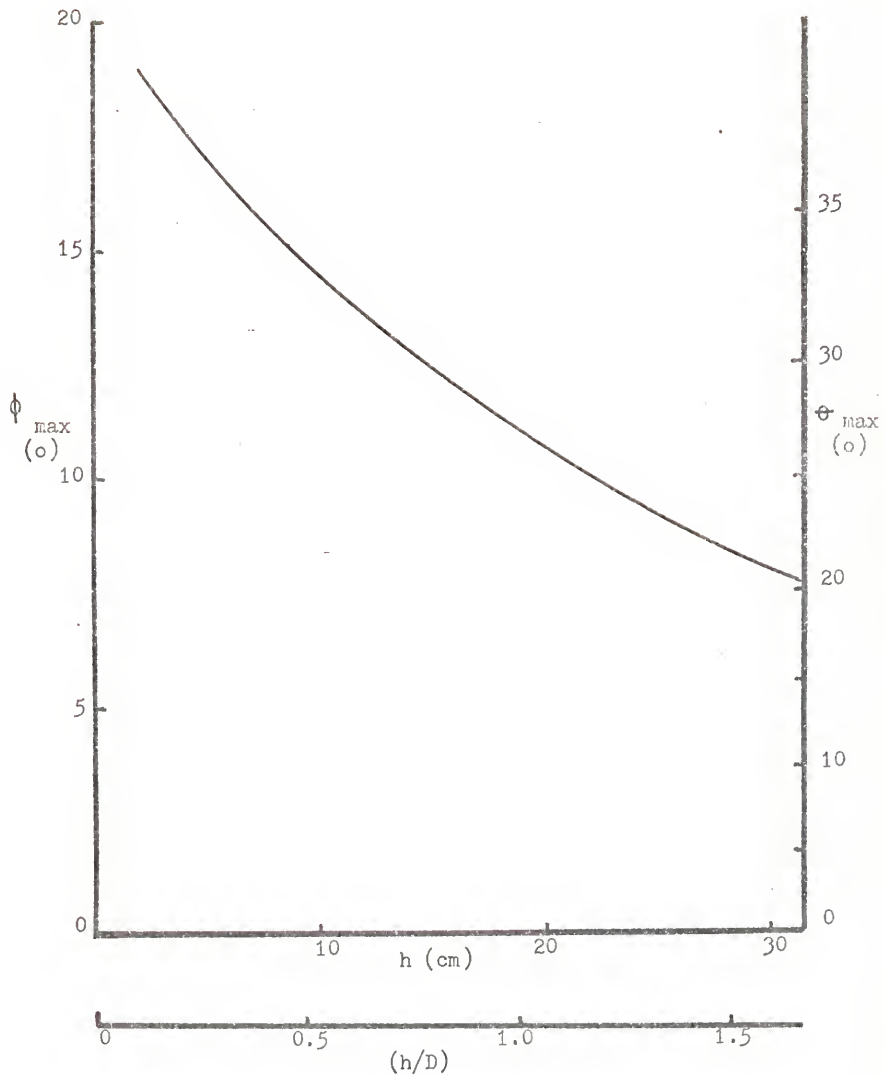


Figure 4: Performance curve for the objective lens. Symbols are defined as: h = height of objective lens above water surface, D = maximum lens barrel diameter, ϕ_{\max} = maximum deflection angle, θ_{\max} = maximum wave slope.

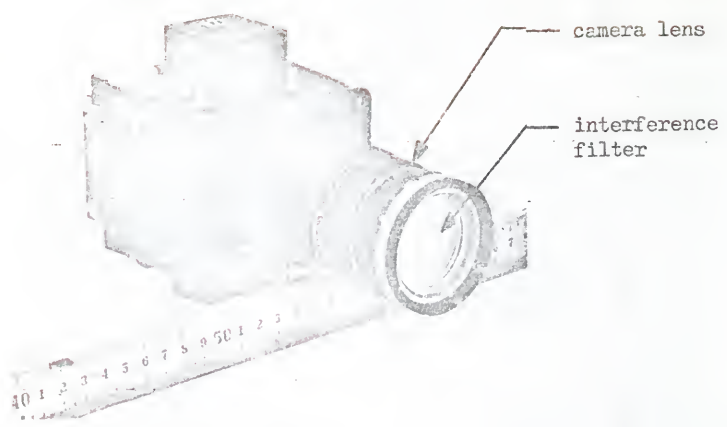
enter the imaging lens module and activate the photodiode. A number of different types of translucent and frosted plastic sheets were tested to find a satisfactory screen material. Scattering lobes for eight different potential screen materials were measured and evaluated. Best results were obtained using a one-eighth-inch-thick sheet of clear acrylic which was roughened to a uniformly frosted appearance by grinding both surfaces with a 400-grit abrasive.

The diffusion screen was placed at the focal plane of the objective lens using a set of adjustable mounting tabs. The mount was made adjustable rather than rigidly fixed to allow for accurate and optimal adjustment of the position of the screen in case the instrument calibration tests indicated that such an adjustment was necessary. Subsequent calibration tests showed that the initial placement of the screen was satisfactory and no further adjustment was necessary.

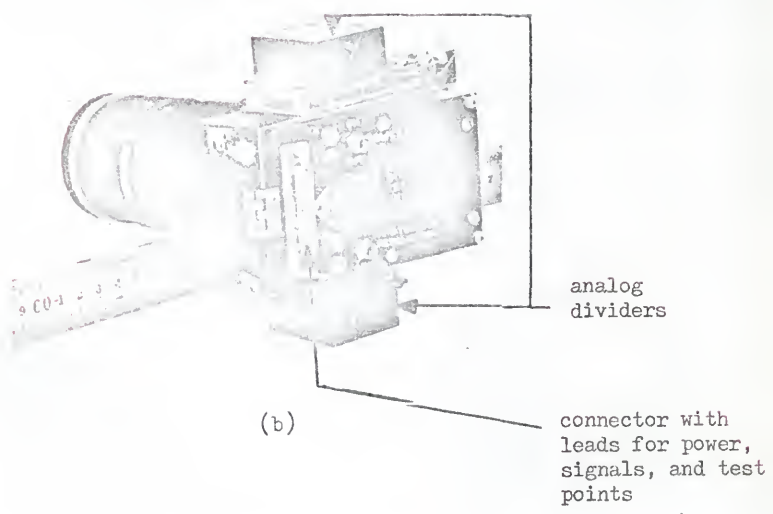
Imaging Lens Module - Optics

The imaging lens module consisted of a 35mm camera lens, the two-dimensional Schottky barrier photodiode, and the electronic amplifier and signal conditioning components. These items were mounted in a common aluminum housing and the entire module somewhat resembled a 35mm camera in appearance. Figure 5 shows front and rear photographs of the imaging lens module.

An interference filter was attached to the camera lens to reduce the effect of background illumination on the output signal from the photodiode. This filter passed the He-Ne laser line at 6328 Ångstroms and had a bandwidth at the half power points of 100 Ångstroms. A 100Å bandwidth was selected because the laser light scattered from the edges of



(a)



(b)

Figure 5 : The imaging lens module; front view, (a), and back view, (b).

the diffusion screen impinged on the surface of the interference filter at relatively large angles of incidence and would not have been passed by a much narrower bandpass filter.¹⁵ The imaging lens was a Super Takumar multi-coated, 55mm focal length, $f/1.4$ camera lens.

Imaging Lens Module - Electronics

The laser beam position sensing transducer was a United Detector Technology continuous Schottky barrier Photodiode Model SC/50 with a 3.56 cm x 3.56 cm active area, shown in Figure 6. Similar devices have been used as radiation tracking transducers, and descriptions of mathematical models for the lateral photoeffect are available in the literature.^{16,17} The photodiode may be operated in either a photoconductive mode, where a reverse bias voltage is applied to the diode junction, or a photovoltaic mode, where no reverse bias is applied to the diode junction. In the photoconductive mode the depth of the depletion region associated with the p-n junction is physically greater than that occurring in the photovoltaic mode of operation. The photoconductive mode features a lower junction capacitance and higher junction resistance which gives rise to a much higher frequency response capability, but also it gives rise to a greater absolute value of noise due to the reversed-bias shot noise. The high value of the junction resistance, approximately 68 megohms at 11 volts reverse bias, allows greater input light intensities to strike the diode surface with no damage due to excessive junction currents. The photovoltaic mode features a higher junction capacitance, lower junction resistance, and a reduced noise level due to the absence of the reversed-bias shot noise. The frequencies dealt with in the present application were low enough to make the effect of the junction

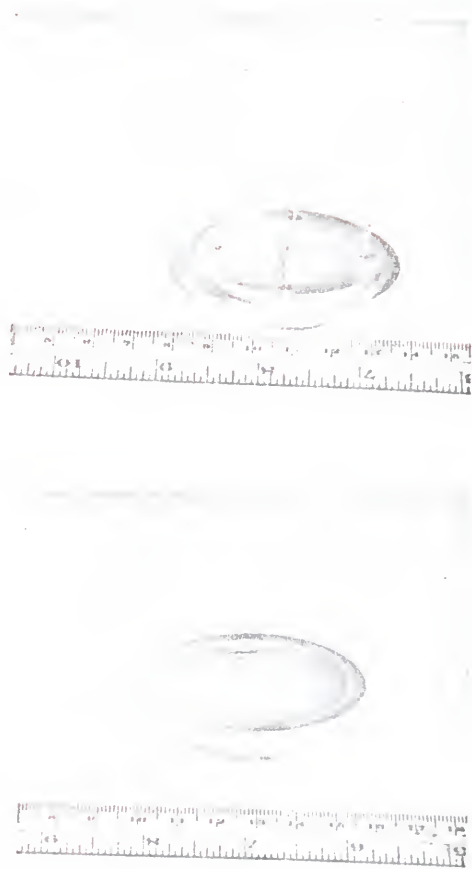


Figure 6 : Two-dimensional Schottky Barrier Photodiode.

capacitance negligible. Both modes of operation were tested, and the photovoltaic mode appeared to be more stable during calibration tests. Therefore, all of the subsequent tests were conducted using the photodiode in a photovoltaic mode of operation.

Figure 7 shows a view of the imaging lens module with the hinged door opened to expose the electronic amplifiers, the regulated power supply and the analog dividers. Originally, commercially available amplifiers were used to amplify the photodiode output, but serious signal drift problems required re-trimming of the amplifier stages every 15-30 minutes. This made practical application of the instrument impossible. The amplifier shown in Figure 7 was a first-generation improvement assembled using low-drift amplifier components. This amplifier allowed operation of the instrument for periods of up to six hours without incurring any serious errors due to electronic amplifier drift. Components for a second-generation improved amplifier were ordered but not delivered in time to be used in any of the tests conducted and reported on in this paper.

Figure 8 shows a block diagram of the electronic amplifier and related signal conditioning components. The photodiode produces four current signals through the four ohmic contacts to the n-type lattice material. Four transconductance amplifiers convert the current signals to amplified voltage signals. The sum and difference amplifiers increase the gain of the signals. The analog dividers normalize each difference signal to the sum signal; the quotients are the x- and y-axis outputs which are insensitive to input light intensity fluctuations at the photodiode. The circuits for the x- and y- channels are virtually identical, and are shown in the schematic diagram in Figure 9.

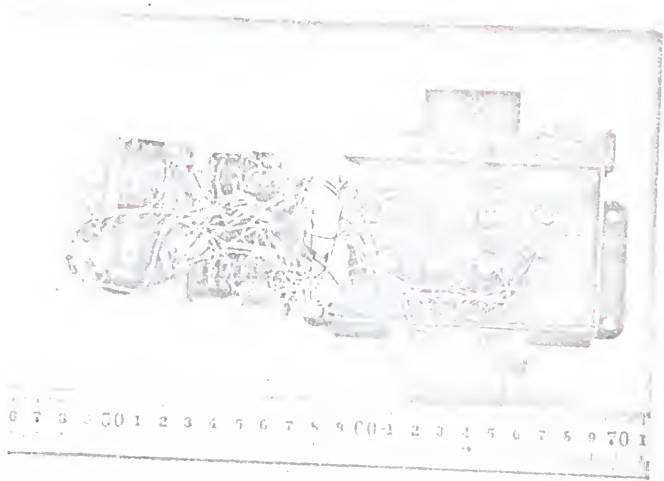


Figure 7 : Electronic amplifiers.

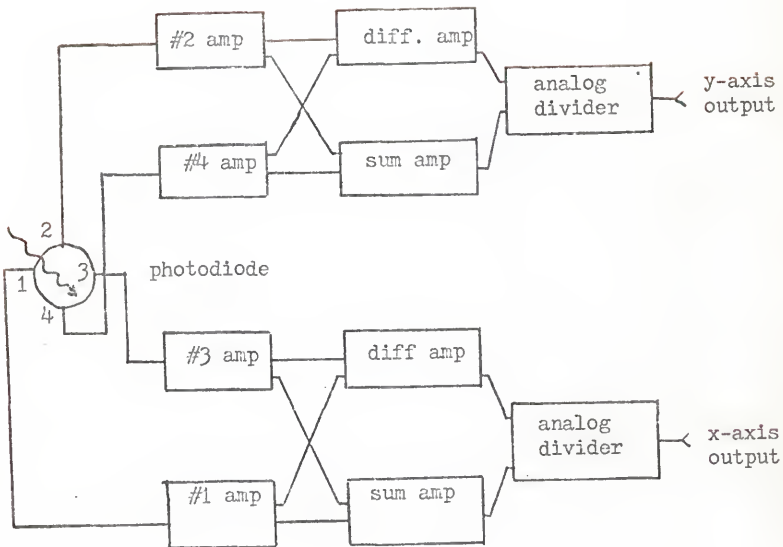


Figure 8 : Block diagram of the electronic amplifier.

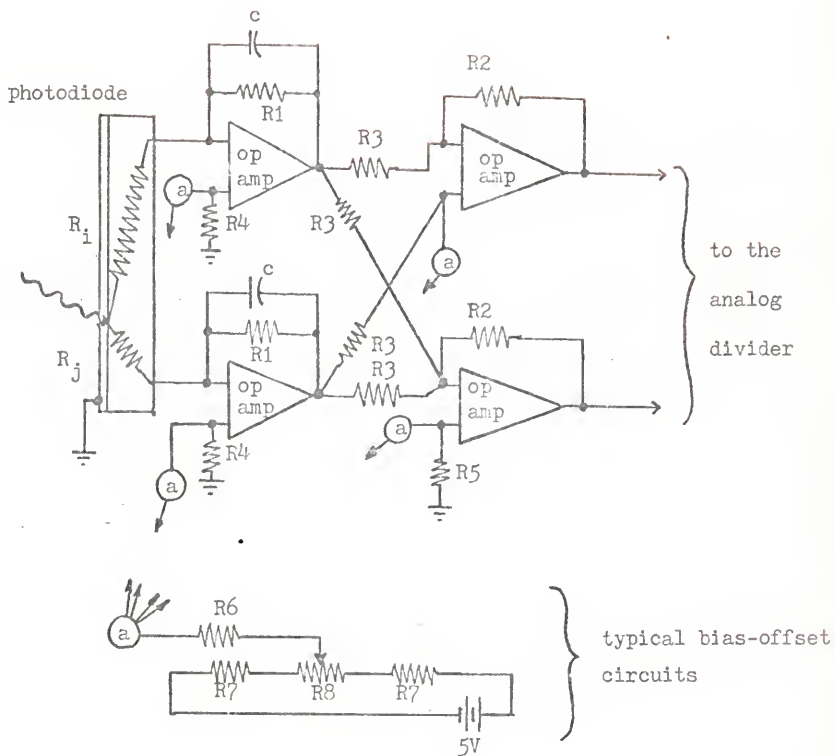


Figure 9 : Schematic diagram of one amplifier channel. Approximate values for resistors, R , and capacitors, c , are: $R_i, R_j = 3.5 \text{ K}\Omega$, $R_1 = .6 \text{ M}\Omega$, $R_2 = .5 \text{ M}\Omega$, $R_3 = 10 \text{ K}\Omega$, $R_4 = 3.5 \text{ K}\Omega$, $R_5 = 5 \text{ K}\Omega$, $R_6 = 1 \text{ M}\Omega$, $R_7 = 50 \text{ K}\Omega$, $R_8 = 50 \text{ K}\Omega$, $c = 1000 \mu\text{f}$.

Low drift analog dividers, manufactured by Analog Devices, were used to perform the signal normalization with respect to the input light intensity. The dividers were trimmed with external potentiometers in the manner suggested by the manufacturer. It was found that normalization accuracy was within 1% when the denominator voltage was in the range -8 v to -4 v. This performance was somewhat degraded as the denominator voltage increased to -10 volts and also an error of 3% was observed as the denominator dropped to -2 v. The normalization error increased very rapidly as the denominator voltage fell below -1.5 v. Therefore, a useful operating range was taken to be any laser intensity that would produce an analog divider denominator voltage in the range -2 v to -10 v.

The analog dividers served as a very convenient means of compensating for variations in the laser light intensity. This was especially useful during calibration of the instrument, since the analog dividers served as real time computers performing the signal normalization. The normalization could have been performed more accurately and over a greater range of laser beam light intensity fluctuations by recording digitized voltages of the sum- and difference-amplifiers and performing the division on a digital computer. However, this method would have been more cumbersome, more time consuming and would have caused a serious delay in the development of the instrument. The effectiveness of the analog dividers in compensating for laser beam intensity fluctuations is illustrated by the oscilloscope traces in Figure 10. Figure 10a shows 60 Hz fluctuations in the sum-amplifier outputs due to powering the laser from a rectified 60-cycle power supply. The x-axis denominator is shown as the upper trace and the y-axis denominator is shown

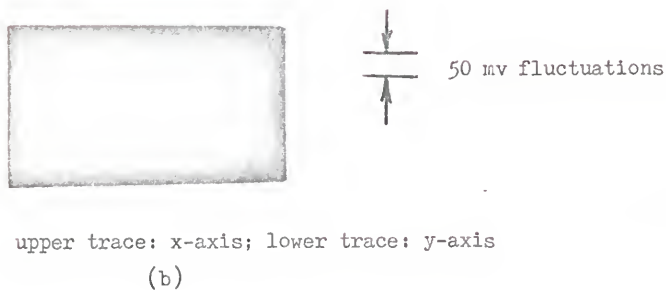
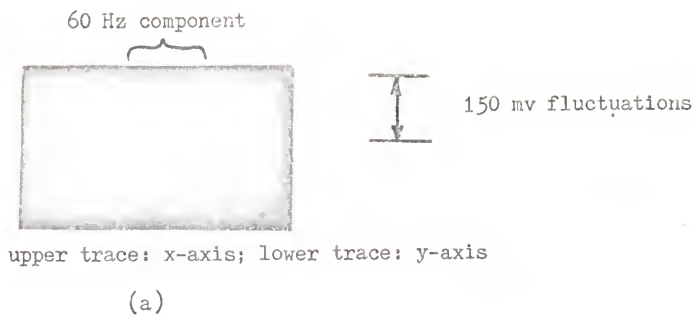


Figure 10: Illustration of the effectiveness of the analog dividers to produce a normalized signal voltage. Typical fluctuations in an un-normalized signal, (a); the normalized signal, (b).

as the lower trace. The numerator signals exhibited the same type of fluctuations with roughly the same amplitudes as those shown for the denominators. Figure 10b shows the result of normalizing the numerator signals to the denominator signals with the analog dividers. Notice the 60 Hz fluctuations are virtually eliminated.

The entire amplifier was found to be very sensitive to small changes in the supply voltage to the amplifier components. A regulated ± 12 v power supply was incorporated to maintain a constant supply voltage to within 5 mv. at room temperature, 75°F , and to within ± 20 mv at temperatures ranging between 45°F and 95°F .

Optical Tube

The optical tube was fabricated using 0.025" aluminum sheet, type 2024-T3. The sheet was rolled and spot welded, and then sealed with room-temperature-vulcanizing silicone rubber. The external surface was coated with a titanium dioxide epoxy resin to provide extra protection from the elements and also to reflect sunlight and aid in maintaining a lower internal tube temperature. The internal surface of the tube was coated with a flat black paint to minimize reflections of scattered light. The main support collar, shown in Figure 3, was an annular ring machined from acrylic plastic stock. The support collar was designed to carry the entire weight of the optical receiver without loading the thin aluminum tube in a lateral direction. This minimized the chance of tube flexure and errors introduced by distortion in the optical alignment of the internal components.

Oceangoing Support Structure

The oceangoing support structure in its final configuration is shown in Figure 11. The structure was designed to withstand loading by six-foot ocean waves with deflections that would produce optical errors no greater than 0.3%. Laboratory tests at three to four times the design loading showed that deflection errors were on the order of $\pm 0.3\%$ to $\pm 0.7\%$ with resonant frequencies for various deflection modes ranging between 1.8 and 3.8 Hz. This indicated that the flexural errors encountered during ocean operation would be less than the 0.3% design value.

The laser carriage had two sets of adjustment screws to aid in establishing the optical axis. The optical receiver carriage featured a double-gimbal support ring to carry the weight of the optical tube. This made optical alignment in the field a relatively simple task, usually requiring no more than 15-30 minutes. A bulls-eye type of bubble level was mounted on the upper horizontal member of the support structure to aid in adjusting the optical axis to the vertical. The level was calibrated to provide a measure of the optical axis deviations from the vertical to $\pm 3^\circ$ in any direction.

The entire oceangoing support structure was designed to be mounted on the servo-driven boom of a wave-follower mechanism. The wave-follower mechanism was designed and built by the Department of Coastal Engineering at the University of Florida. It is a semi-portable structure that may be mounted on the ocean floor in thirty feet of water as shown schematically in Figure 12. The hydraulically driven boom has a dynamic range of ± 2 meters about the mean water level and operates such that an attached instrument package maintains a relatively constant height above the water surface.

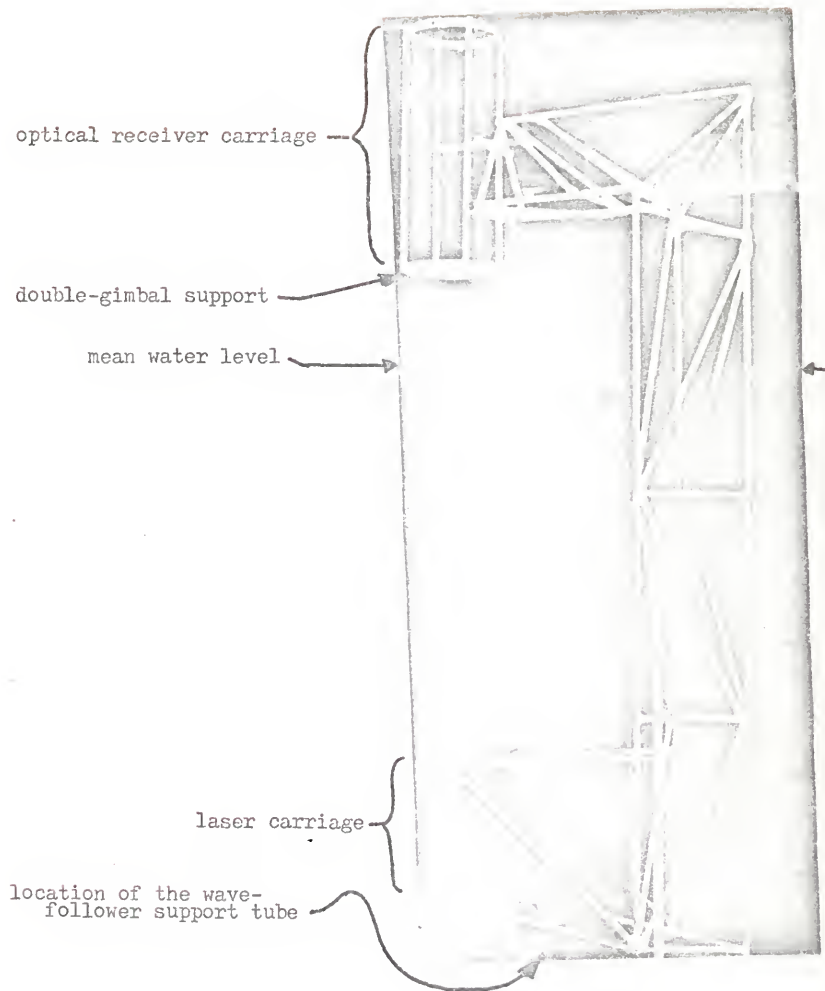


Figure 11: The oceangoing support structure.

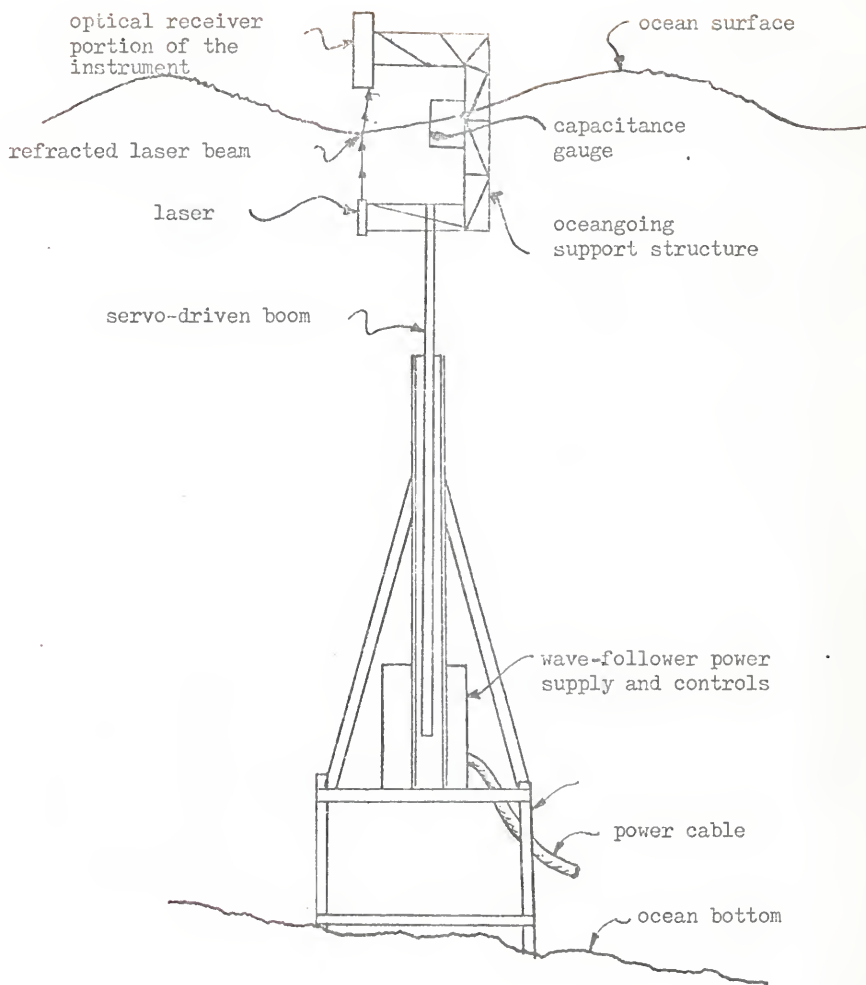


Figure 12 : Sketch of the wave slope instrument during ocean operation.

CHAPTER III
THEORETICAL PERFORMANCE AND
OPERATING CHARACTERISTICS OF THE INSTRUMENT

Introductory Remarks

Calibration of the instrument consists of measuring the amplified output voltage signals for each of the two orthogonal axes of the two-dimensional photodiode as functions of the laser beam deflection angle, ϕ , and the azimuthal angle, ψ . The deflection angle, ϕ , is then related to the wave slope, θ , via equation (6) and the orientation of the surface normal, as shown in Figure 1, may be determined. If the signal normalization process discussed earlier is to be performed on a digital computer, then four voltages must be recorded for each value of ϕ and ψ , i.e. the sum-amplifier output and the difference-amplifier output for each of the two orthogonal axes is required. If the analog divider is used to perform the normalization, then only two voltages, the analog divider outputs, are required for each value of ϕ and ψ . Calibration using the analog dividers was by far the more convenient method of calibration during the development of the instrument, but it was subject to uncertainties in calibration due to some sensitivity of the analog dividers to the value of the denominator signals.

Calibration Using the Analog Dividers

Figure 13 shows a photograph of the calibration set up in the optics laboratory. A 2 mw polarized HeNe laser was mounted at right angles to the optical bench which was used to support the optical receiver portion of the wave slope instrument. The laser beam was directed through a Polaroid filter to a right angle prism used to reflect the beam parallel to the axis of the optical bench. The axes of the optical bench and the reflected laser beam were aligned prior to mounting the instrument in an optical bench cradle. The cradle was then adjusted such that the optical axis of the instrument coincided with the path of the laser beam. The Polaroid filter could be rotated to vary the light intensity into the instrument and thus simulate attenuation of the laser beam due to absorption. The prism was used to simulate refraction at water surface. Changes in the deflection angle, ϕ , could be simulated by rotating the prism. This was accomplished by mounting the prism on a leveled turntable that could be rotated about a vertical axis. The accuracy of the turntable movement was approximately 0.02° . Changes in heights above the water surface could be simulated by sliding the instrument cradle along the optical bench.

Figure 14 shows a typical plot of the calibration data. The x-axis and y-axis analog divider output voltages are denoted by Q_x and Q_y , respectively. Solid lines connect data points corresponding to $\Psi = \text{constant}$ and broken lines connect data points corresponding to $\phi = \text{constant}$. The points were generated by first setting the null signal position, and then stepping the simulated deflection angle, ϕ , in 2° -increments across the entire surface of the objective lens. The output voltages from the analog dividers were read using a digital voltmeter and recorded. The

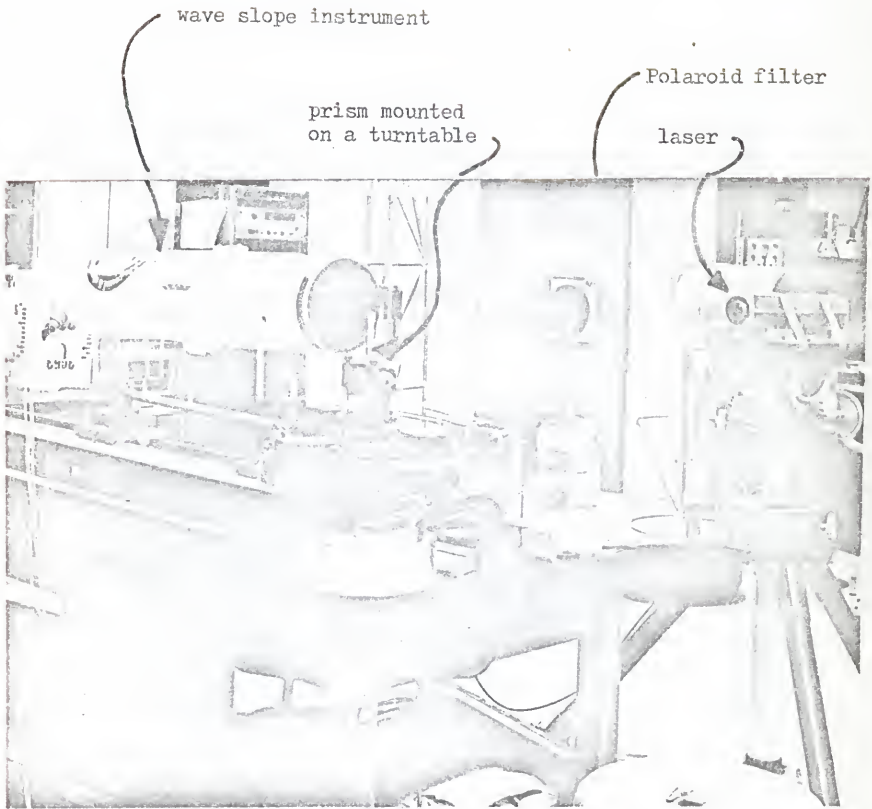


Figure 13 : The calibration set up in the optical laboratory.

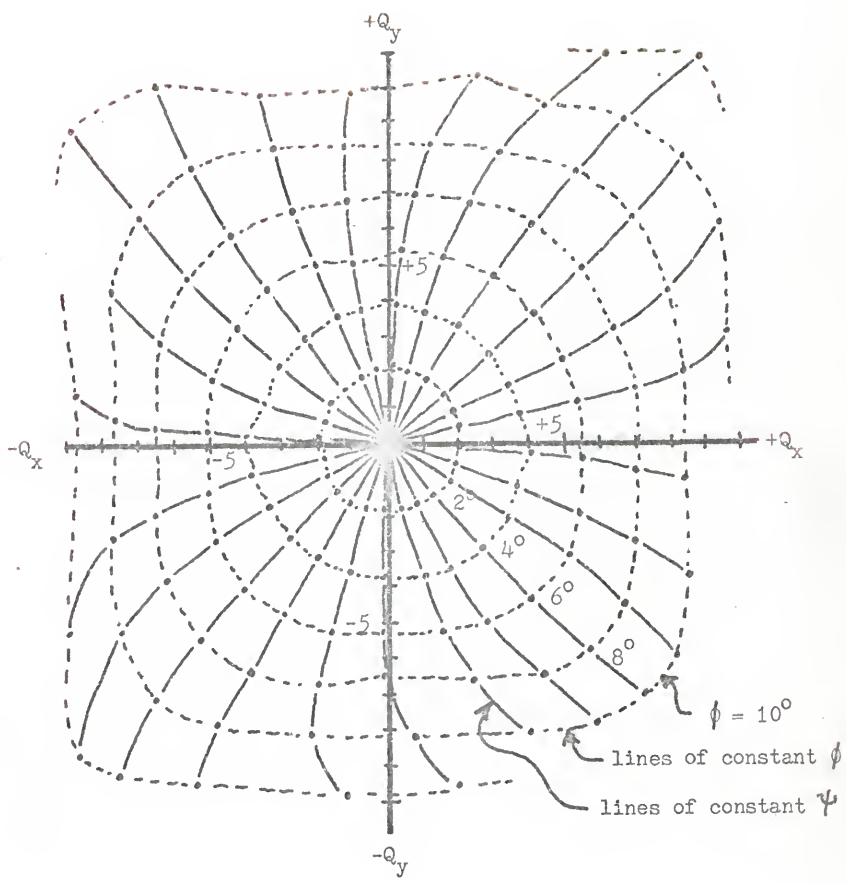


Figure 14: A typical plot of calibration data obtained using the analog divider. Q_x and Q_y have units of volts.

instrument was then rotated approximately 15° about the optical axis and the procedure repeated.

A major concern in the application of the instrument is the repeatability of calibration data. It was found that at a constant temperature the calibration data were consistent to within 2-3%. However, a change in temperature of $10-15^{\circ}$ led to calibration variations on the order of 10-20%. Nearly all of this variation could be accounted for by temperature dependent changes in the offset voltage. The amplified offset voltages as a function of temperature are shown in Figure 15. The temperatures were measured inside the optical tube at the physical location of the amplifiers with the optical tube sealed in its ocean-going configuration. A gas-tube thermometer with a dial indicator was used to make the temperature measurements. The thermometer and its location relative to the amplifiers is shown in Figure 16. Calibration data for various optical tube temperatures were taken in the laboratory. In the field, the tube temperature during the test was monitored so that an appropriate set of calibration data could be applied to the resulting test data. After correcting for temperature changes, the maximum uncertainty in the calibration was estimated to be on the order of $\pm 7\%$.

Evaluation of Optical Aberrations

Optical aberrations result when rays from a common point in the object space enter the lens at different locations and fail to come to a common point of focus at the location of the image point determined from Gaussian or paraxial approximations. Any rays which deviate from the Gaussian approximation are thought of as some sort of aberration. Lengthy treatments of aberrations may be found in any of several good

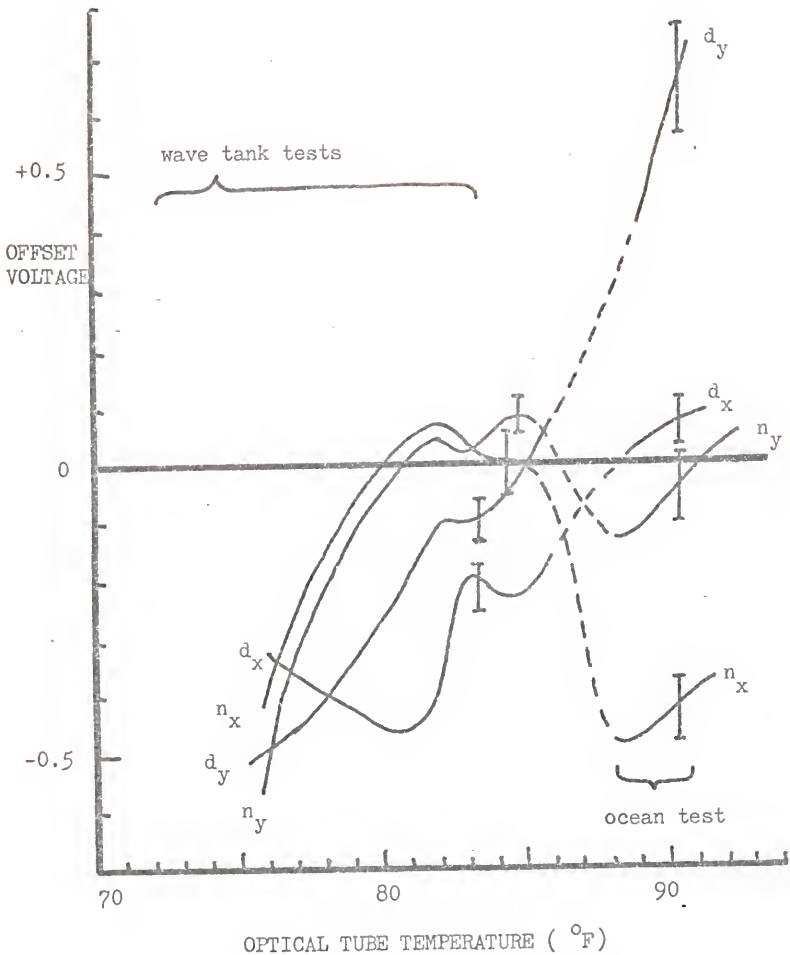


Figure 15 : Offset voltages measured with respect to the amplifier outputs. Numerator and denominator voltages are denoted by n and d, respectively. Subscripts refer to axes of the photodiode. Error bars indicate the scatter of data points; the broken line segments represent temperatures at which no data points were generated.

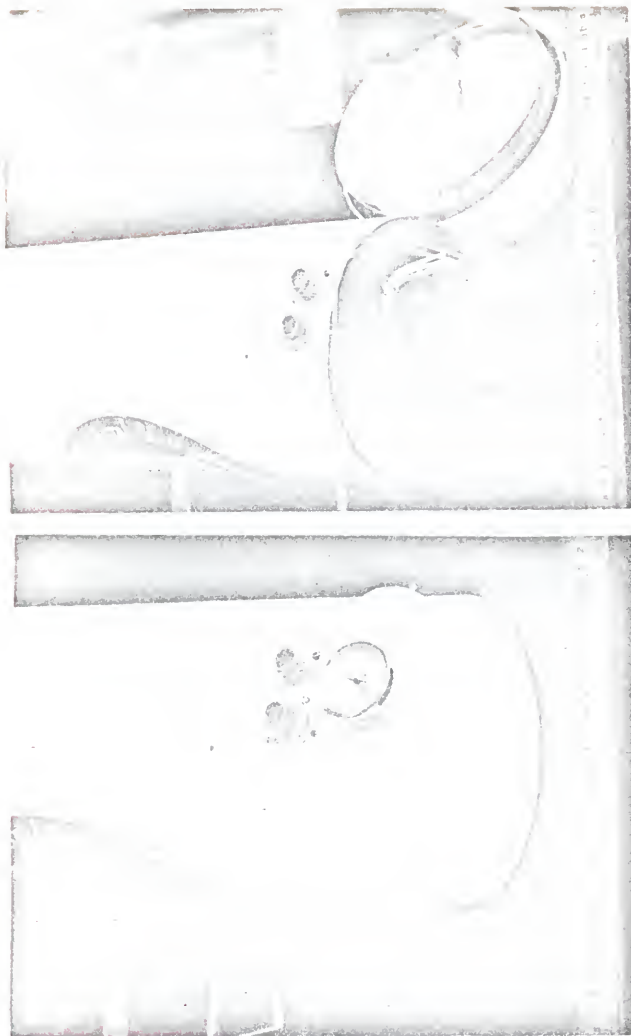


Figure 16 : Photographs showing the location of the optical-tube thermometer relative to the amplifiers in the imaging lens module.

reference books on optics.^{14,18,19}

The effects of optical aberrations associated with the objective lens were evaluated by an indirect method. Since optical aberrations may affect both the location of a point in the image plane and the sharpness of the image, and since any significant aberrations would lead to measurable variations in the instrument's output signals, the output of the instrument itself was used to estimate the severity of optical aberrations.

The laser beam was treated as a "fat light ray." This test ray was allowed to enter various portions of the objective lens while keeping the deflection angle, ϕ , and the azimuthal angle, ψ , constant. During these variations the output signals were monitored to detect any significant changes. In practice, the angle ψ was held constant by avoiding any rotation of the optical tube after the optical axes of the instrument and the laser beam were aligned on the optical bench as shown previously in Figure 13. The deflection angle, ϕ , was then varied such that the laser beam moved over the entire surface of the objective lens. The x- and y-axis output voltages were recorded and plotted as a function of ϕ . The distance between the prism and the objective lens was varied keeping ψ constant and the deflection angle, ϕ , was again varied through its full useful range. Again the x- and y-axis voltages were recorded and plotted as a function of ϕ . The entire procedure was repeated a third time at still a different value for the separation between the prism and the objective lens of the instrument. This process allowed the beam with a specific orientation, (ϕ, ψ) to enter the objective at different radial locations on the surface of the lens. If aberrations had been important, the data points corresponding to common values of

ϕ and ψ would have changed noticeably. This was not the case, however. The voltages corresponding to common values of ϕ and ψ were repeatable to within the value of the noise in the analog divider outputs. Thus, it was concluded that the effects of optical aberrations were negligibly small and completely masked by the noise in the electronics.

The Frequency Response of the Instrument

The frequency response of the instrument was determined by physically chopping the laser beam with a rotating mechanical aperture. The laser beam was positioned to produce a null signal output from the analog dividers when the beam was allowed to enter the objective lens. Blocking the laser beam with a mechanical stop caused the denominator signals to the analog dividers to go to zero, thus the divider became saturated at the maximum divider output voltage. By switching the laser on and off at high frequencies the frequency response of the entire system, from photodiode to divider output, was evaluated. The results showed that the frequency response of the entire system was flat to frequencies well above 400 Hz. Since all of the data gathered with the instrument were filtered to eliminate frequencies in excess of 100 Hz before digitizing the analog signals, it was concluded that the frequency response of the instrument was flat throughout its useful operating range.

Wavelength Response Characteristics

Cox has shown that the finite dimensions of the spot on the water through which all rays must pass on their way to the detector form a

"low-pass" filter to the signal.¹ Measurable wavelengths must satisfy the inequality $\lambda \geq 6.8r_0$ where r_0 is the radius of the spot size, and λ is the resolvable wavelength. This resolution criterion is applicable to systems in which the light intensity is uniform across the spot. The following analysis considers the case where the light intensity varies across the spot in the form of a two-dimensional Gaussian distribution function.

A first approximation to the wave slope instrument's response to a finite-sized laser beam assumes that the photodiode is sensitive only to the centroid of the laser beam focused on the diffusion screen. This is a reasonable assumption because the spot on the diffusion screen is usually small and well defined for wavelengths satisfying the Cox criteria.

This assumption, plus the use of the linear relationship between the radial displacement of a ray on the diffusion screen, ρ , and the deflection angle, ϕ , as given in equation (7) allows the analysis to be simplified. It follows that $\bar{\rho} = \bar{\phi}$, where $\bar{\phi}$ is defined as the deflection angle corresponding to refraction at a plane surface which results in a centroid located at $\bar{\rho}$.

The variation between $\bar{\phi}$, the measured deflection angle and ϕ_0 , the deflection angle of the central ray in the laser beam was examined first. Next, the fact that the photodiode is not strictly sensitive to the laser beam centroid was dealt with and an error associated with the spreading of the light intensity distribution about the centroid was estimated.

Errors Due To A Finite-sized Laser Beam

The theory of operation presented earlier was based on the refraction of a single ray of laser light. For the single ray case, the wave slope,

51
 θ , is related to the deflection angle, ϕ , by equation (6):

$$(6) \quad \theta = \arctan \left\{ \frac{\sin \phi}{n - \cos \phi} \right\}$$

where n is the relative index of refraction for water.

In the case of a laser beam of finite dimensions, the beam may be considered as a bundle of rays distributed over a finite region about the optical axis. Here, the optical axis is placed at the centroid of the laser beam as it emerges from the laser cavity. In general, rays penetrating the water surface at different locations will encounter different wave slopes and hence give rise to different deflection angles. A measure of the wave slope at the optical axis is still desired, but it becomes necessary to work with a mean deflection angle, $\bar{\phi}$, rather than a single deflection angle at the optical axis. A value for the measured wave slope, θ_m , is defined as

$$(9) \quad \theta_m = \arctan \left\{ \frac{\sin \bar{\phi}}{n - \cos \bar{\phi}} \right\} .$$

Since $\bar{\phi}$ will generally vary from the value of the deflection angle at the optical axis, ϕ_0 , the measured wave slope, θ_m , will generally be different from the true wave slope occurring at the optical axis, θ_0 . Therefore, an uncertainty or error in wave slope measurement may be defined as

$$(10) \quad \epsilon = \theta_m - \theta_0 .$$

It is desirable to describe the behavior of the error, ϵ , as a function of the laser beam parameters and the configuration of the water surface at the test site. This is a problem of considerable complexity, but a first-order estimate of the behavior of the error may be made following the introduction of a few simplifying assumptions. These assumptions are

- (1) Geometric optics are assumed to be adequate for a satisfactory description of the system, i.e. diffraction effects are considered negligible and ray tracing techniques may be employed.
- (2) The coherence properties of the laser beam are assumed unimportant, thus interference effects are negligible and a light intensity distribution rather than an electromagnetic wave amplitude distribution is associated with the laser beam.
- (3) The laser beam below the surface of the water is assumed to be perfectly collimated, i.e. consisting of a bundle of perfectly parallel rays.
- (4) The light intensity distribution in the laser beam is assumed to be a Gaussian distribution centered about the optical axis.
- (5) The surface of the water is assumed to be accurately described by a linear combination of sinusoidal plane waves of varying wave numbers and with varying directions of propagation.

The fifth assumption allows the surface amplitude to be described as

$$(11) \quad z(x,y,t) = \sum_{i=0}^{\infty} a_i \sin(\vec{k} \cdot \vec{r} - w_i t + \xi_i)$$

where the subscript "i" refers to the i^{th} -component of an infinite series of plane waves, \vec{k} is a three-dimensional wave number, \vec{r} is a radius vector measured perpendicular to the optical axis, w is the radian frequency of the wave component, t is the time, and ξ is an arbitrary phase offset measured at time $t=0$. The x-, y-dependence is introduced by the use of a cylindrical coordinate system:

$$(12) \quad \begin{aligned} z &= z \\ x &= r \cos \psi \\ y &= r \sin \psi \end{aligned}$$

where ψ is an azimuthal angle measured with respect to the positive x-axis. Figure 17 illustrates the configuration for the i^{th} -wave component propagating in the ψ azimuthal direction. The Gaussian laser beam is centered about the optical axis at $(x=0, y=0)$ and is directed in the positive z-direction.

To simplify the analysis, consider a single wave component with wave number k , where the cartesian reference frame has been rotated such that the wave component travels along the y-axis, and ξ has been set to zero. Under these conditions, the surface is described by

$$(13) \quad z = a \sin(ky - wt)$$

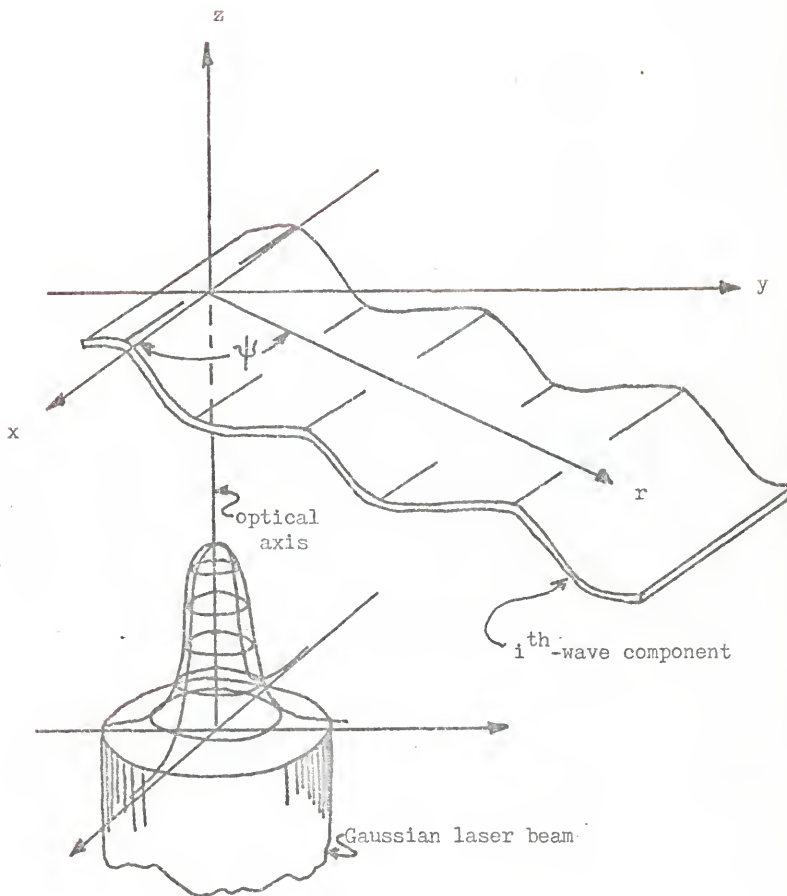


Figure 17 : Configuration for the i^{th} -wave component and the Gaussian laser beam.

where the subscript "i" has been dropped. This type of analysis is consistent with that of Cox in estimating the wavelength response characteristics.¹

The wave slope of this simplified model is then

$$(14) \quad \theta = \frac{dz}{dy} = ak \cos(ky - wt) \quad .$$

In cylindrical coordinates

$$(15) \quad \theta = ak \cos(kr \sin(\psi) - wt) \quad .$$

The deflection angle, ϕ , is found by Snell's Law,

$$(16) \quad \sin(\phi + \theta) = n \sin \theta,$$

to be

$$(17) \quad \phi = \arcsin(n \sin(\theta)) - \theta$$

which becomes, upon substituting equation (15) into equation (17),

$$(18) \quad \phi(r, \psi) = \arcsin \left[n \sin(ak \cos(kr \sin(\psi) - wt)) \right] \\ - ak \cos(kr \sin(\psi) - wt) \quad .$$

The deflection angle, $\phi(r, \psi)$, is specified at each point (r, ψ) throughout the xy-plane by equation (18). The Gaussian laser beam weights

each of these points by a factor

$$(19) \quad p(r, \psi) = \frac{\sigma^2}{\pi} e^{-\sigma^2 r^2}$$

where the factor $\frac{\sigma^2}{\pi}$ was introduced to make the weight function normalized in the sense that

$$(20) \quad \iint_{-\infty}^{+\infty} p(r, \psi) \, dA = 1 \quad .$$

The expectation value of ϕ , or the mean value of ϕ is $\bar{\phi}$ and is defined by

$$(21) \quad \bar{\phi} = \langle \phi \rangle = \iint_0^{\infty} \int_0^{2\pi} \phi(r, \psi) p(r, \psi) r \, dr \, d\psi \quad .$$

Substituting equations (18) and (19) into equation (21) gives the expression

$$(22) \quad \bar{\phi} = \iint_0^{\infty} \int_0^{2\pi} \frac{\sigma^2}{\pi} e^{-\sigma^2 r^2} \arcsin \left[n \sin(ak \cos(kr \sin(\psi) - wt)) \right] r \, dr \, d\psi \\ - \iint_0^{\infty} \int_0^{2\pi} \frac{\sigma^2}{\pi} e^{-\sigma^2 r^2} ak \cos(kr \sin(\psi) - wt) r \, dr \, d\psi \quad .$$

Referring back to equation (17) and Snell's Law, it is seen that the first integral in equation (22) has no obvious physical significance, but the second integral in equation (22) is clearly the mean value of the wave slope relative to the Gaussian weight function supplied by the laser beam intensity distribution. Integration of the second integral is relatively straightforward, giving²⁰

$$(23) \quad \int_0^{\infty} \int_0^{2\pi} \frac{r^2}{\pi} ak e^{-\sigma^2 r^2} \cos(kr \sin(\psi) - wt) r dr d\psi = ak \cos(wt) e^{-k^2/4\sigma^2}$$

Since $ak \cos(wt)$ is the slope evaluated at the optical axis, the weighted mean slope is simply the slope at the optical axis weighted by the factor $\exp(-k^2/4\sigma^2)$.

Integration of the first integral in equation (22) could not be accomplished in closed form so that a numerical scheme was necessary for evaluation.

The numerical integration scheme used an approximation to the Gaussian weight function as illustrated in Figure 18. The central cylinder and each of the annular-ring segments carried equal flux and were thus equally weighted. These equally weighted segments were then divided by a number of radials such that each of the resulting sub-segments were equally weighted. The equally weighted sub-segments were then replaced by equally weighted delta-functions. The delta-functions were located at the centers of each sub-segment, with the center being defined by a mean radial distance and a mean azimuthal angle for each of the sub-segments. The approximation shown in Figure 18 provides a 16-point approximation to the Gaussian distribution. In practice, 360-point and 1800-point approximations were used.

Note that the solution to the second integral of equation (22) as expressed in equation (23) is a function of three parameters: ak , the maximum wave slope; wt , the phase of the plane wave; and the ratio k/σ . This suggested a change in the radial integration variable for the first integral of equation (22) from r to $r\sigma = \rho$. After making this variable

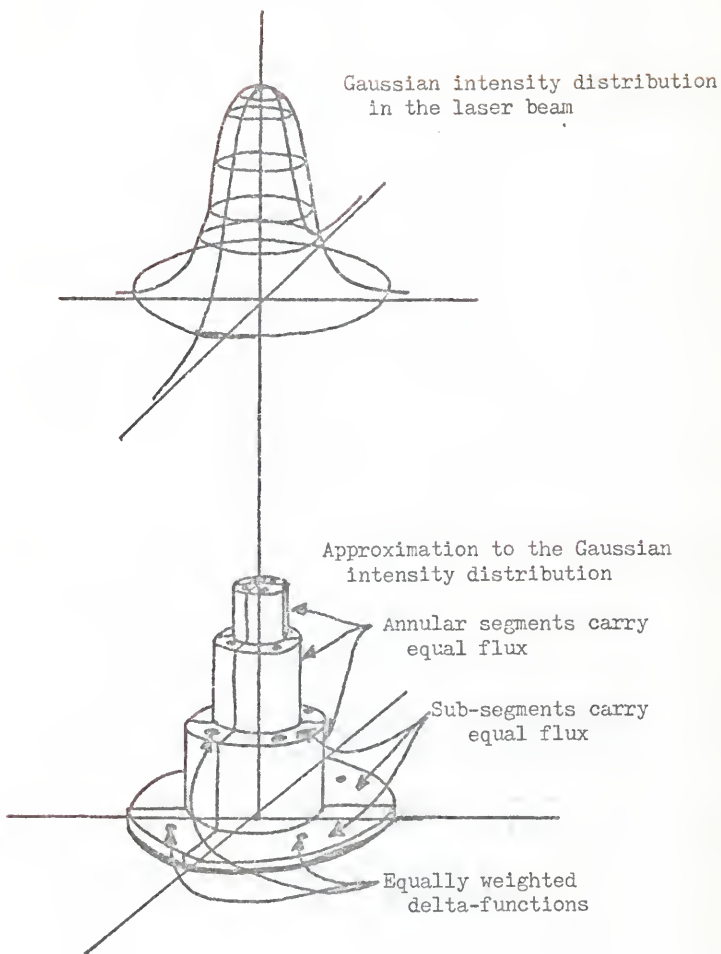


Figure 18 : Approximation to the Gaussian intensity distribution used in the computer error analysis.

change and re-defining the locations of the delta-functions in the Gaussian weight function approximation, the mean deflection angle, $\bar{\phi}$, became

$$(24) \quad \bar{\phi} \approx \left\{ \sum_{i=1}^m \sum_{j=1}^n \frac{1}{mn} \delta(\beta_i, \psi_j) \arcsin \left[n \sin(ak \cos(k/\sigma) \right. \right. \\ \left. \left. \sin(\psi_j) - wt) \right] \right\} - ak \cos(wt) e^{-k^2/4\sigma^2}.$$

Equation (24) was then evaluated on an IBM 370 digital computer for various values of the parameters ak , wt , and k/σ . The same computer program also evaluated $\bar{\theta}_m$ as expressed in equation (9) and the wave slope error, ϵ , as defined in equation (10).

At this point it is convenient to digress momentarily to clarify the significance of σ and k/σ . The laser beam parameter, σ , is a measure of the radius of the Gaussian intensity distribution given in equation (19). The radius of a Gaussian laser beam usually refers to the $1/e^2$ point of the beam, i.e. the radius at which the intensity reaches approximately 0.14 of the maximum intensity. Calling this radius r_0 , it is seen from equation (19) that σ may be defined as

$$(25) \quad \sigma = \sqrt{2}/r_0$$

and has units of reciprocal length. Note that since σ is a function of r_0 , it is also a function of distance from the output window of the laser cavity for a diverging beam.

A plane wave of wave number k has an associated wavelength given by

$$(26) \quad \lambda = 2\pi/k$$

Thus it is seen that the ratio of the water wavelength to the laser beam radius may be expressed as

$$(27) \quad \lambda/r_0 = \frac{2\pi}{\sqrt{2} (k/\sigma)} = \frac{4.44}{(k/\sigma)}$$

Equation (27) is plotted in Figure 19.

The parameter k/σ was convenient to use in the computer analysis, but wavelength-to-laser beam radius ratios are difficult to visualize using k/σ as a parameter. Therefore, whenever k/σ is used as a parameter, the conversion to units of λ/r_0 is indicated.

The computer calculated wave slope errors indicated that the greatest absolute error occurred at phase $wt=0$, i.e. at the point of greatest wave slope. Figure 20 shows the error in wave slope for various values of the parameter ak plotted as a function of parameter k/σ . In all cases, the error is associated with the worst-error case occurring at $wt=0$.

Figure 21 shows the percent error in wave slope measurement for $ak \approx 5^\circ$ and $ak \approx 45^\circ$ plotted as a function of the parameter k/σ . Again, these values correspond to the worst-error case of $wt = 0$. It is seen that a 10% error in wave slope measurement occurs at $k/\sigma = 0.65$ ($\lambda/r_0 = 6.83$) for $ak \approx 5^\circ$, and $k/\sigma = 0.76$ ($\lambda/r_0 = 5.84$) for $ak \approx 45^\circ$.

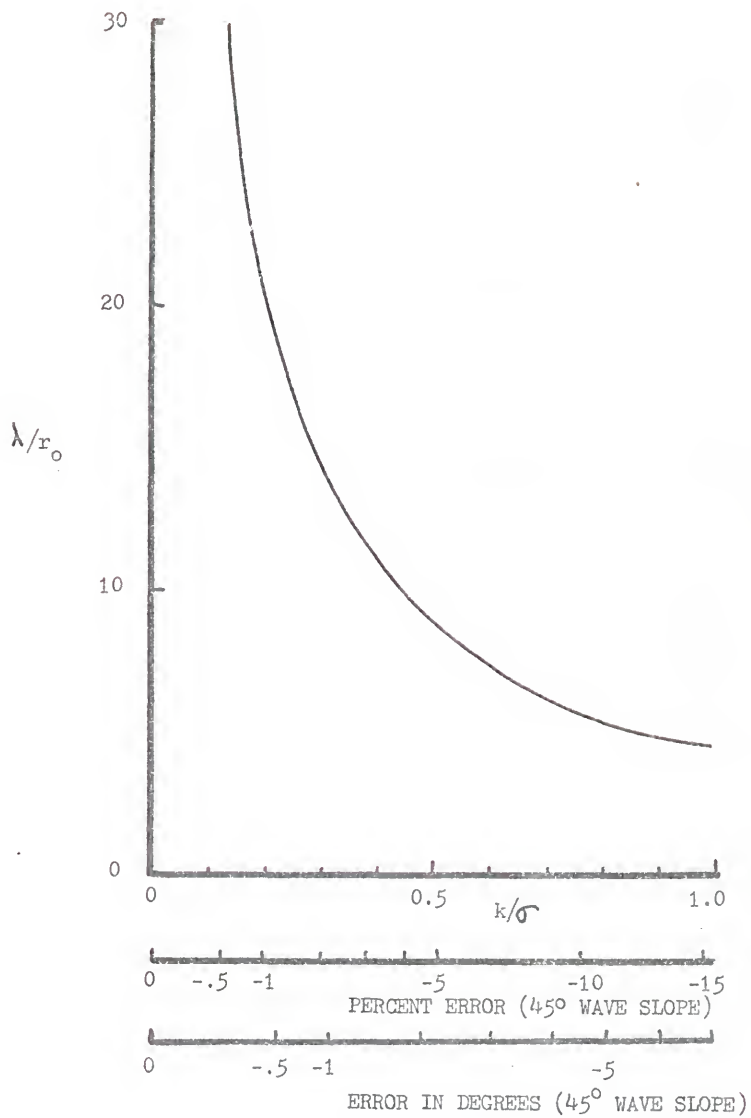


Figure 19 : λ/r_0 as a function of parameter k/σ . Additional abscissas are scaled to show the percent error and the error measured in degrees for the case of a maximum wave slope of 45° .

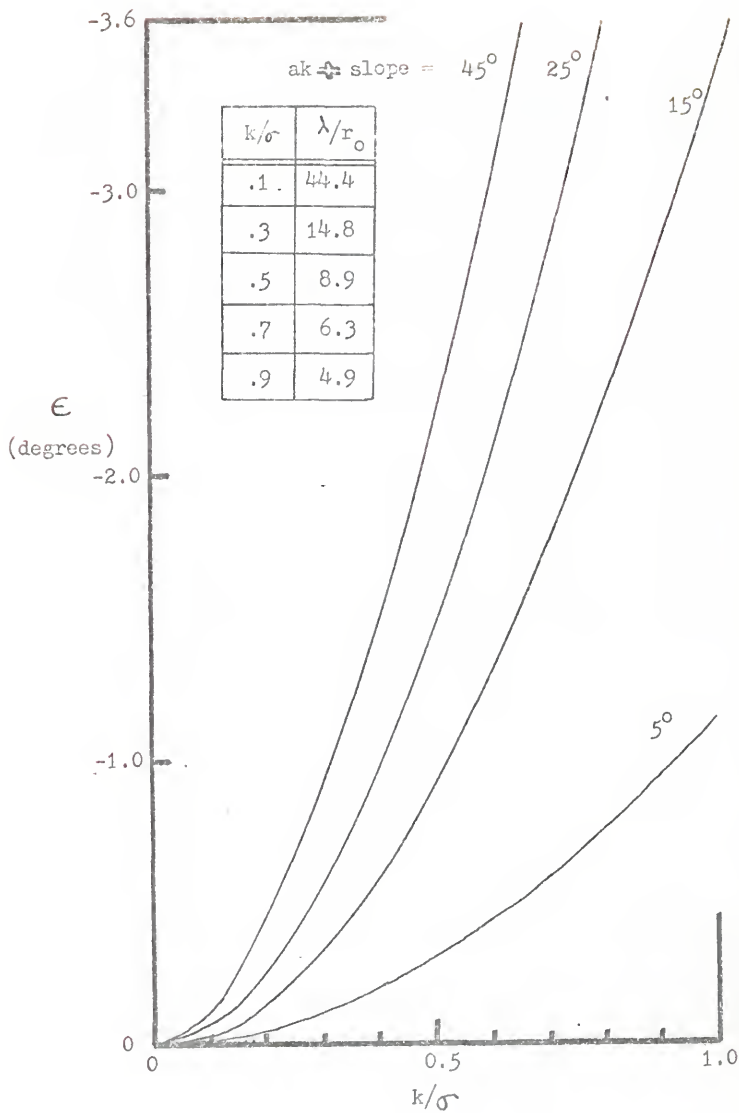


Figure 20 : Error in wave slope measurement, ϵ , as a function of parameter k/σ , at $wt = 0$, for various values of parameter ak .

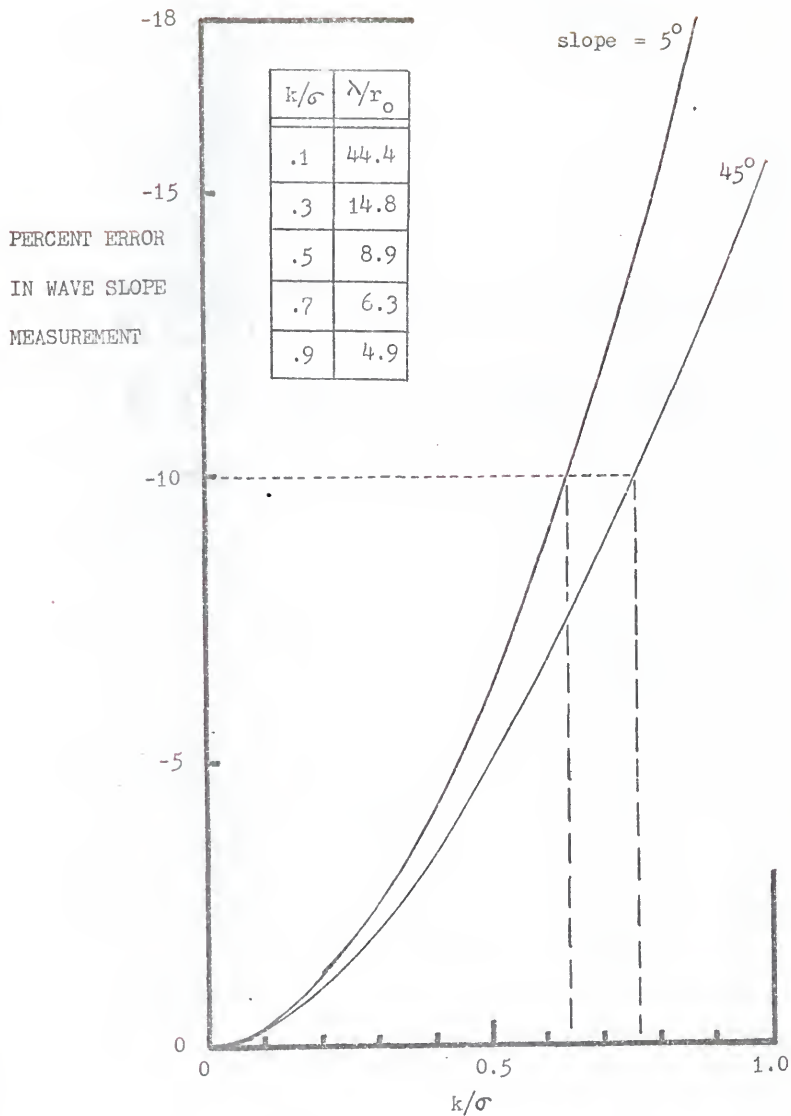


Figure 21 : Percent error in wave slope measurement as a function of parameter k/σ , for $wt = 0$ and $ak \approx 5^\circ, 45^\circ$.

Taking $k/\sigma = 0.7$ ($\lambda/r_0 = 6.34$) as a representative value corresponding to a 10% error at $wt = 0$, the behavior of the error as the phase of the wave changed from zero degrees to 90° was examined for various values of the wave slope parameter, ak . The computer evaluations of the error, based on a 360-point Gaussian approximation, are plotted in Figure 22. The most noteworthy features in Figure 22 are the noticeable inflection points in the curves for slopes $> 30^\circ$, and the actual change in sign of the error for values of slope approaching 40° . The sign change was found to be a physically observable phenomenon and not an artifact introduced by the computer analysis. The error in wave slope measurement was found to be satisfactorily modeled by the expression

$$(28) \quad \epsilon(wt) = \epsilon_1(ak, k/\sigma) \cos wt + \epsilon_2(ak, k/\sigma) \cos 3wt$$

where the coefficients ϵ_1 and ϵ_2 are functions of the parameters ak and k/σ . For certain values of these parameters, the coefficient ϵ_2 may become greater than ϵ_1 , thus shifting a substantial portion of the error from a frequency w to a frequency $3w$. For example, a steep sinusoidal wave having a slope of 45° , when measured with a Gaussian laser beam with radius $r_0 = 0.157 \lambda$, would produce a 4.3% error at radian frequency w and a 4.3% error at a radian frequency $3w$. The result is an erroneous indication that the wave of radian frequency w contains a superposed ripple component of radian frequency $3w$. Growth of the coefficient ϵ_2 is very rapid as the slope exceeds 30° , but for slopes of 35° or less, greater than 80% of the error is associated with the coefficient ϵ_1 , the "in phase" error component. Since the instrument described

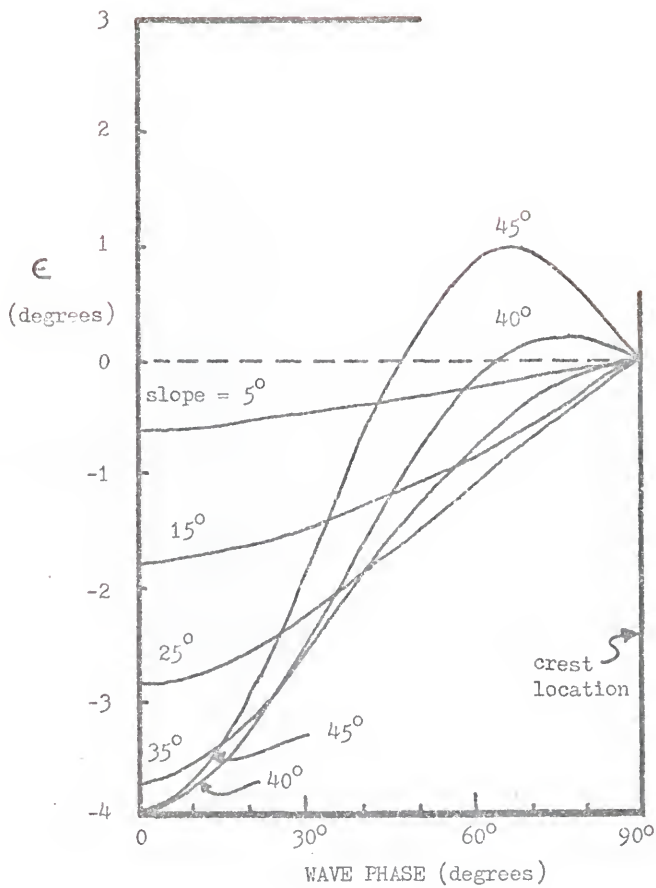


Figure 22 : Error in wave slope measurement, ϵ , as a function of wave phase for various values of maximum wave slope and for $k/c = 0.7$ ($\lambda/r_0 = 6.34$).

in this paper is not suitable for measuring slopes in excess of 35° at reasonable heights above the water surface, the problem of errors shifting to higher frequencies may be considered of negligible importance.

The quantity defined by the symbol ϵ should be taken as an error rather than a correction factor to be applied to the wave slope data, unless the wave number spectrum of the wave field is accurately known. This is true because the orbital velocity or the fluid velocity associated with the gravity waves destroys the one-to-one correspondence between the observed signal frequency, f , and the wave number, k , as is discussed presently.

A simple wave field consisting of a single sinusoidal plane wave propagating through the test site would produce a wave slope signal of a single frequency, f , related to the radian frequency, w , by the expression

$$(29) \quad f = w/2\pi .$$

Phillips gives the radian frequency of a wave as

$$(30) \quad w = (gk + \gamma k^3)^{1/2}$$

where g is gravitational acceleration, k is the wave number of the wave, and γ is a constant determined from the surface tension and the density of the water.²¹ He also shows that the wave number of a short wave changes in the presence of a long wave according to the expressions

$$(31) \quad k = k_0 + \delta k$$

$$(32) \quad \delta k = k_0(U/c)$$

where k is the wave number of the short wave in the presence of a long wave, k_0 is the wave number of the short wave in the absence of a long wave, δk is the observed change in the wave number of the short wave, U is the fluid velocity of the long wave, and c is the phase velocity of the long wave. It is readily found that an approximate expression for the radian frequency of a short wave in the presence of a long wave is

$$(33) \quad \omega \approx (gk_0 + \gamma k_0^3 - gk_0 U/c + 3\gamma k_0^3 U/c)^{1/2}$$

The observed signal frequency may then be written as

$$(34) \quad f \approx (1/2\pi)(gk_0 + \gamma k_0^3 + gk_0 U/c + 3\gamma k_0^3 U/c)^{1/2}$$

At the crest of a long wave, U is a maximum positive value and the observed signal frequency for the short wave is greater than the frequency expected when no long wave is present. When no long wave is present, $U = 0$ and equation (34) degenerates to equation (30). At the trough location of the long wave, U is a maximum negative value and the observed frequency is less than that occurring when no long wave is present.

27

Determining the fluid velocity, U , in the presence of several randomly superposed long waves of varying wavelengths becomes complex and intractable for practical purposes. Thus, the one-to-one correspondence between an observed signal frequency and a unique wave number as expressed in equations (29) and (30) is destroyed by the presence of long waves. Surface currents, whether generated by the action of wind on the water, tides, or other mechanisms, also complicate the problem by introducing additional fluid velocity components.

The error in the wave slope measurement, as discussed above, is not the only source of error due to a finite-sized laser beam, although it may be considered dominant. A secondary error, δ , is associated with the type of sensor used, i.e. the continuous, two-dimensional, Schottky barrier photodiode. This secondary error results from the fact that the photodiode is not truly sensitive to the centroid of the light intensity distribution striking the surface of the photodiode. That is, a delta-function distribution and a Gaussian distribution, each having the same centroid location and carrying the same amount of flux, will generally produce different output signals from the photodiode. Taking the delta-function distribution as a reference distribution, the error, δ , may be defined as a fractional error by

$$(35) \quad \delta = (S - S_{\text{ref}}) / S_{\text{ref}}$$

where S is the output signal for a general distribution of light on the surface of the photodiode and S_{ref} is the output signal for a

25

delta-function distribution, it being understood that both distributions have the same centroid location.

A conservative estimate to the magnitude of δ for the case of a Gaussian laser beam of radius r_0 interacting with a sinusoidal plane wave of wavelength $\lambda = 6.34 r_0$ and a maximum wave slope of 35° was found to be $\delta = -0.019$, i.e. a -1.9% error. Referring back to Figure 21, it is seen that the percent error due to the error ϵ is approximately -10% for the case $\lambda = 6.34 r_0$ and slope = 35° . Thus the ϵ -error accounts for more than 80% of the total error. For the case of a slope of 35° and $\lambda = 4.9 r_0$, the δ -error increases to approximately -5.6% and the ϵ -error increases to approximately -15%. Thus it is seen that the influence of the ϵ -error becomes more and more apparent as the ratio λ/r_0 decreases, contributing significantly to the total error associated with the use of a finite-sized laser beam as the wavelength, λ , approaches the dimension of the laser beam.

CHAPTER IV WAVE TANK TEST

The instrument was used in a series of one-dimensional wave tank tests conducted at the University of Florida's Wave Tank Facility in late March, 1975. The laser was mounted horizontally, outside of the wave tank roughly 35 cm below the mean water level. The laser beam was directed through a plate glass window to an underwater-mounted prism where the beam was deflected upward along the vertical. The wave slope instrument was mounted with the objective lens 8 cm above the mean water level. Optical alignment was performed under calm-water conditions with the x- and y-axis channels directed in the crosswind and downwind directions, respectively.

Figure 23 shows samples of the downwind channel signal for the cases: no mechanical wave, wind speed of 11.9 m/sec; 2 second, 2.5 cm amplitude mechanical wave, wind speed of 11.9 m/sec; and 2 second 5 cm amplitude mechanical wave with wind speed of 8.2 m/sec. In all cases the upper time series is the downwind channel output signal and the lower time series is a capacitance gauge output which gives an indication of the phase of the wave. Mechanical waves and wind go from right to left. Some features to note are

- (1) the development of a 4 Hz wave structure due to the action of the wind with no mechanical wave,
- (2) the 4 Hz wind generated wave undergoes an apparent frequency increase to 4.4 Hz at the crest of the 2.5 cm mechanical



Figure 23 : Sample records from the wave tank tests.

- wave, and decreases to 3.6 Hz in the trough,
- (3) the frequency modulation of the wind generated wave over the 5 cm mechanical wave, with frequencies approaching 10 Hz at the crest and 4.4 Hz in the trough,
 - (4) the concentration of ripple activity on the downwind face of the wind generated waves as indicated by the 80-100 Hz components in the wave slope instrument's time series record,
 - (5) maximum wave slopes of 11° - 14° in the case of the 8.2 m/sec wind speed, and 20° - 23° in the case of the 11.9 m/sec wind speeds.

Phillips has shown that the wave number and the wave amplitude of short waves increase at the crest of long waves and decrease in the trough.²¹ This gives rise to greater wave slopes with higher observable frequencies at the crest of the long wave and lesser wave slopes with lower frequencies at the trough. The time record for the 5 cm mechanical wave, as shown in Figure 23, is entirely consistent with Phillips' prediction.

At high wave slopes the laser beam would deflect off the objective lens and a signal dropout occurred. Dropout was detected by a zero denominator signal. Minimal dropout occurred during these tests and there are no examples of dropout in the sample records shown.

Figure 24 shows the frequency spectra of the mean square slope for the three sample records plotted on log-log scales.* The energy units

*The spectra presented were provided by Mr. Allen Reece of the Department of Coastal Engineering at the University of Florida. The spectra were generated using a Fast Fourier Transform computer program developed by Robinson.²²

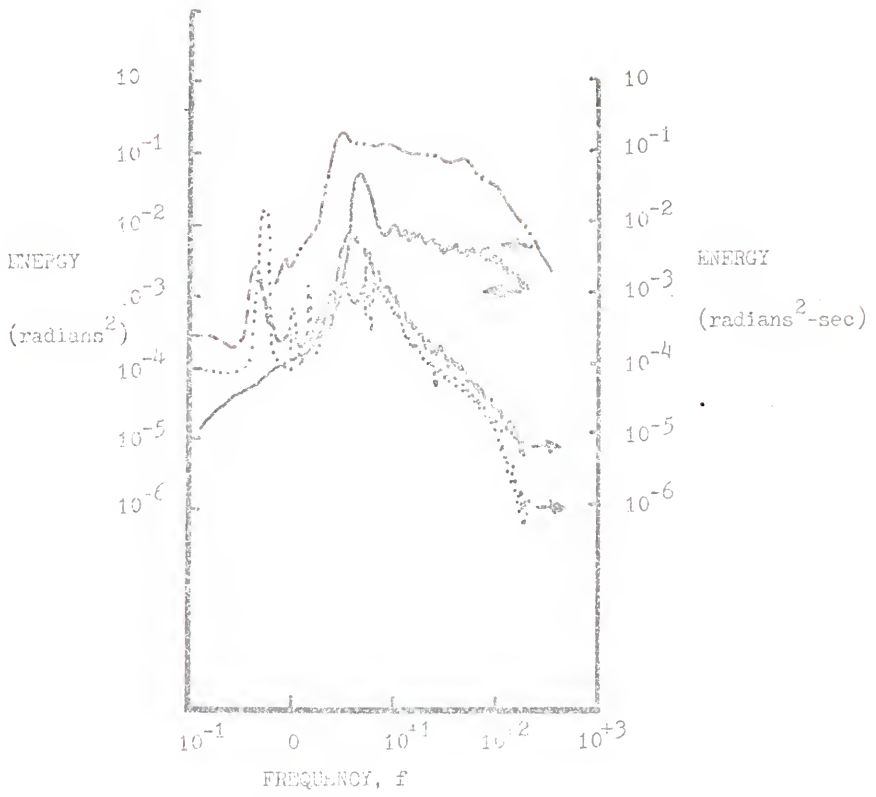


Figure 24 : Frequency spectra of the mean square slope.

for the 2.5 cm and 5.0 cm mechanical wave cases are in radians²-sec and the appropriate ordinate appears to the right of the figure. The spectrum for the case of no mechanical wave was multiplied by the frequency in order to compare with the spectrum of Cox which is also shown in the figure.¹ The units of these latter cases are radians² and the appropriate ordinate appears to the left of the figure. Note the increase in the 0.5 Hz component as the mechanical wave amplitude increases. Also note the decrease in the 4 Hz component as the mechanical wave amplitude increases. Presumably, this is due to a frequency spreading effect as discussed earlier in connection with the modification of short waves by the fluid velocity associated with long waves. The reason for the order of magnitude difference between the Cox spectrum and the present spectrum is still under active investigation. Some possible reasons for the difference are the presence of a light oil slick in the University of Florida Wave Tank; the Cox fetch was 2.14 m while the present tests were conducted at a fetch of 9.1 m; Cox was sensitive to light intensity fluctuations and also made linearizing assumptions concerning the light intensity distribution across the spot and the modulation of the intensity due to changing wave slopes; mm and sub-mm ripples may have affected the present measurements due to excessive spreading of the refracted laser beam.

CHAPTER V
OCEAN TESTS

The ocean wave slope measurements were made on May 29, 1975, at a location off the coast of Marineland, Florida. A shrimp boat carried the auxiliary power supply units and the data acquisition station. The wave follower mechanism was set in thirty feet of water. A standpipe with an attached ladder was mounted next to the wave-follower boom to facilitate the installation and removal of instrument packages. Figure 25 shows a photograph of the shrimp boat's position relative to the test site.

The instrument carried separate battery power packs for the electronic amplifiers and the Coherent Radiation Model 80-2s submersible laser. Wave slope signals were hard-wired to the data acquisition center. Figure 26 shows the instrument in operation during the ocean test. The immediate test site was protected from the effects of sunlight by an opaque plastic sheet.

Sample records of the ocean test data are shown in Figure 27. Traces (a) and (b) are the y- and x-axis outputs, respectively. Trace (c) is the x-axis denominator signal which was monitored to identify regions of signal dropout. Trace (d) is a wave staff record indicating the crest and trough locations of the 60 cm ocean swell.

The ocean test data were not processed for several reasons:

- (1) The recording anemometer was lost during preliminary tests when a standpipe supporting the instrument was snapped by ocean currents at a pipe coupling.



Figure 25 : Photograph of the shrimp boat's position relative to the ocean test site.

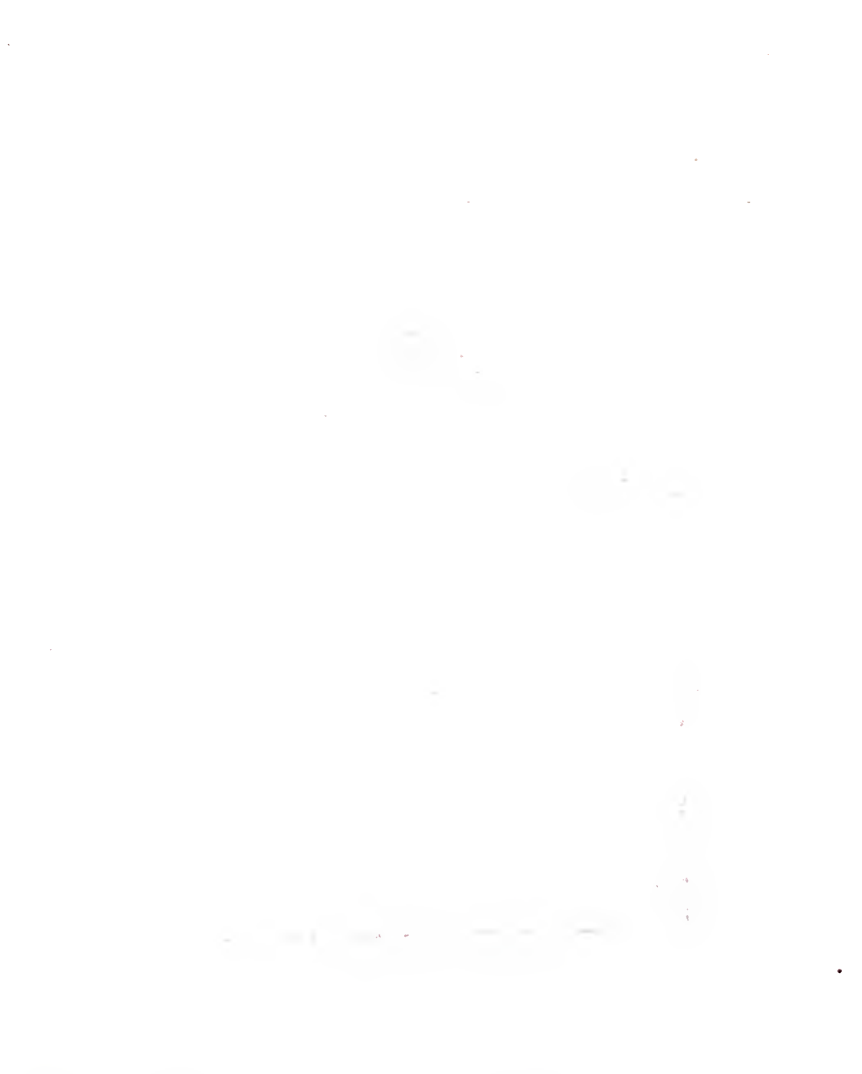


Figure 26 . The instrument in operation during the ocean test.

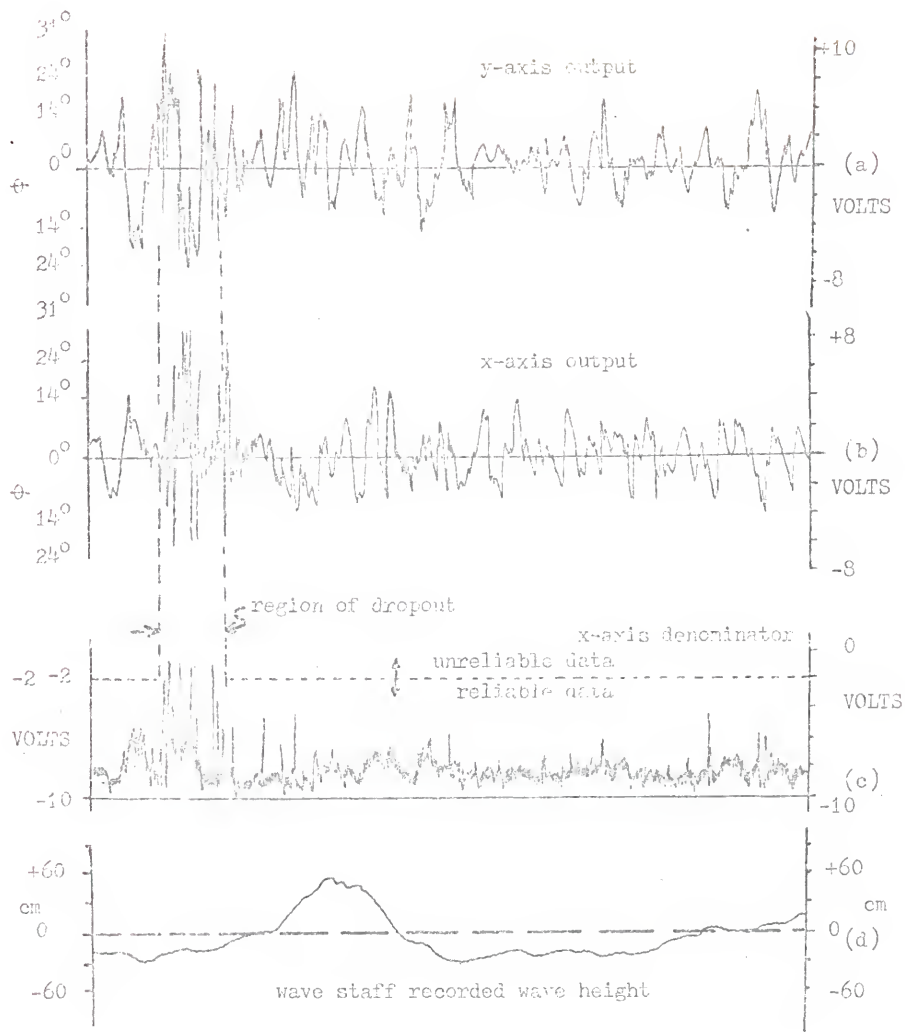


Figure 27 : Sample records of ocean test data.

- (2) The test site was cluttered with interference during the test. Swells reflected from the shrimp boat, and the test site was directly on the lee side of the shrimp boat.
- (3) The standpipe with attached ladder was too close to the test site and swells frequently slapped the ladder causing serious wavelet reflections.
- (4) Portions of the record displayed considerable dropout due to fish in the laser beam. On several occasions a group of 20 - 30 small fish took turns filing through the laser beam. Fish dropout was easily identified by long periods of zero denominator signal.
- (5) The cost of computer time required to analyze the ocean data was considerable. Since no direct application could be made of the data analysis due to items (1) - (4) above, the ocean data were not processed.

CHAPTER VI
SUMMARY

The instrument described here has shown several significant advances in obtaining continuous time records of wave slopes occurring at a point. The data are two-dimensional and compatible with the nature of the water surface. The instrument has demonstrated the ability to function as both a laboratory instrument and a portable field unit. It is insensitive to wave height and light intensity fluctuations, thus making it suitable for measuring ripples in the presence of swell in either clear or turbid water conditions. The instrument has an increased slope measuring capacity and a demonstrated capability for daytime field use not shown by previous instruments.^{15,23} Errors were based on equations that were not linearized, thus giving a more realistic description of wavelength resolution than that of Cox.¹

For the tests conducted, the maximum errors due to wavelength resolution were estimated to be -2.5% at $\lambda = 1.33$ cm, -5% at $\lambda = .80$ cm, -11.9% at $\lambda = .57$ cm and -20.5% at $\lambda = .44$ cm.

CHAPTER VII CONCLUDING REMARKS

It is felt that the instrument described here is the most advanced wave slope measuring instrument of its type to date. Further improvements, such as greater wave slope measuring capability, lower temperature-dependent calibration errors, and greater wavelength resolution are well within reach. Greater field utility may result from an added signal telemetry module and a simplified calibration scheme which may be applied in the field if necessary. The instrument's performance is expected to increase markedly by incorporating a field lens in place of the diffusion screen. Data processing should become less time consuming by interfacing the data acquisition system with a high speed digital computer. A third-generation instrument should provide wave amplitude information in addition to the two-dimensional wave slope information, thus providing a more complete time history of the surface at a point.

REFERENCES

1. Cox, Charles S., "Measurements of Slopes of High-Frequency Wind Waves," Journal of Marine Research, 16, 3, 1958, pp. 199-225.
2. Stillwell, Denis, Jr., Optical Analysis for the 1971 ARPA Tower Experiment, NRL Report 7445, May, 1971.
3. McGoldrick, Lawrence F., "Resonant Interactions Among Capillary-Gravity Waves," Journal of Fluid Mechanics, 21, 2, 1965, pp. 305-331.
4. Valenzuela, Y. R., M. B. Haug and J. C. Daley, "Ocean Spectra for the High-Frequency Waves as Determined from Airborne Radar Measurements," Journal of Marine Research, 29, 2, 1971, pp. 69 - 84.
5. Hollinger, James P., "Passive Microwave Measurements of Sea Surface Roughness," IEEE Transactions on Geoscience Electronics, GE - 9, 3, July 1971, pp. 105 - 109.
6. Daley, J. C., "Wind Dependence of Radar Sea Return," Journal of Geophysical Research, 75, 38, Nov. 1970, pp. 7823 - 7833.
7. Phao, Gilbert N., George W. Kattaman, and John A. Guinn, Jr., "Radiative Transfer in the Earth's Atmosphere and Ocean: Influence of Ocean Waves," Applied Optics, 14, 8, Aug. 1975, pp. 1925 - 1936.
8. Pilon, P. O., "Deterministic of Ocean Surface Descriptors Using Sea Photo Analysis Techniques," NRL report 7574, July, 1973.
9. Wu, Jih, "Slope and Curvature Distributions of Wind-Disturbed Water Surface," Journal of the Optical Society of America, 61, 7, July, 1970, pp. 852 - 856.
10. Cox, Charles, and Walter Mack, "Statistics of the Sea Surface Derived from Sea Clutter," Journal of Marine Research, 13, 2, 1954, pp. 198 - 227.
11. Cox, Charles, and Walter Mack, "Measurement of the Roughness of the Sea Surface from Photographs of the Sun's Glitter," Journal of the Optical Society of America, 44, 11, November 1956, pp. 838 - 850.
12. Topp, G. R. C. Anderson and G. S. Chordin, "Laser Instrument for Measuring Water Surface Slopes," Applied Optics, 12, 4, April, 1973, pp. 1041 - 1044.

13. Scott, John C., "An Optical Probe for Measuring Water Wave Slopes," Journal of Physics E: Scientific Instruments, 7, 1974, pp. 747 - 749.
14. Klein, Miles V., Optics, John Wiley and Sons, New York, 1970.
15. Edging Optics Catalog, 1979-1975, The Edging Corporation, Cambridge, Mass., 1973. pp. 182 -183.
16. Allen, D. A., "An Analysis of the Radiation Tracking Transducer," IRE Transactions on Electron Devices, September, 1962, pp 411 - 416.
17. Lucovsky, G., "Photoeffects in Nonuniformly Irradiated p-n Junctions," Journal of Applied Physics, 31, June 1960, pp. 1088 -1095.
18. Born, Max, and Emil Wolf, Principles of Optics, Pergamon Press, Oxford, 1970.
19. Conrady, A. E., Applied Optics and Optical Design, Dover Publications, New York, 1957.
20. Gradshteyn, I. S., and I. M. Ryzhik, Tables of Integrals, Series, and Products, Academic Press, New York, 1965.
21. Phillips, J. M., The Dynamics of the Upper Ocean, Cambridge University Press, London, 1969.
22. Robinson, E. A., Multichannel Time Series Analysis with Digital Computer Programs, Holden-Day, New York, 1967.
23. Prettyman, Clinton E. and Mary D. Cernak, "Time Variation of the Rough Ocean Surface and its Effect on an Incident Laser Beam," IEEE Transactions on Geoscience Electronics, GE-7, 4, October, 1969, pp. 235-243.

BIOGRAPHICAL SKETCH

Charles S. Palm was born July 20, 1943 in Detroit, Michigan. He spent the first 22 years of his life in the Detroit area and gained industrial experience as an apprentice electrician for the Ford Motor Company. He moved to Florida in 1965 and started his college education. Mr. Palm received a BSASE and an MSASE at the University of Florida in August, 1970 and March, 1973, respectively. Work toward a Ph.D. was completed in August, 1975.

Mr. Palm is married to the former Martha Emelyn Bagwell and has a three-year-old son, Karl.

Mr. Palm plans to continue his work in the research and development of optical instrumentation.

I certify that I have read this study and that in my opinion it conforms to acceptable standards of scholarly presentation and is fully adequate, in scope and quality, as a dissertation for the degree of Doctor of Philosophy.



Roland C. Anderson, Chairman
Professor of Engineering Sciences

I certify that I have read this study and that in my opinion it conforms to acceptable standards of scholarly presentation and is fully adequate, in scope and quality, as a dissertation for the degree of Doctor of Philosophy.



Omar H. Sbeidin
Professor of Engineering Sciences

I certify that I have read this study and that in my opinion it conforms to acceptable standards of scholarly presentation and is fully adequate, in scope and quality, as a dissertation for the degree of Doctor of Philosophy.



David T. Williams
Professor of Engineering Sciences

I certify that I have read this study and that in my opinion it conforms to acceptable standards of scholarly presentation and is fully adequate, in scope and quality, as a dissertation for the degree of Doctor of Philosophy.



Ulrich H. Kurzweg
Associate Professor of Engineering
Sciences

I certify that I have read this study and that in my opinion it conforms to acceptable standards of scholarly presentation and is fully adequate, in scope and quality, as a dissertation for the degree of Doctor of Philosophy.

Paul Urope
Professor of Environmental
Engineering Sciences

This dissertation was submitted to the Graduate Faculty of the College of Engineering and to the Graduate Council, and was accepted as partial fulfillment of the requirements for the degree of Doctor of Philosophy.

August, 1975



Dean, College of Engineering

Dean, Graduate School

